

3. Results and discussion

Various physicochemical techniques being evident for preparation of GO, successful functionalization of the amino-based moiety; Schiff base ligand and immobilization of metal ions are described here. A catalysts synthesized by modifying –OH groups of GO is commonly represented as $M(L)_n-f-GO$ (i.e. $CoL-f-GO$, $VOL-f-GO$, $CuL-f-GO$).

3.1. Characterization of –OH functionalized catalysts

3.1.1. FTIR analysis

Fig. 3.1 shows the FTIR spectra of GO, A-*f*-GO, L-*f*-GO (L = Schiff base ligand) and $M(L)_n-f-GO$ ($M = VO^{4+}$, Co^{2+} , Cu^{2+}) which validates the successful oxidation of graphite into GO. Besides this, functionalization of oxidative debris, particularly hydroxyl groups, with APTMS is also corroborated by FTIR analysis. FTIR spectrum of GO exhibited characteristic vibrations at 3389 cm^{-1} , 1722 cm^{-1} , 1623 cm^{-1} and 1057 cm^{-1} are attributed to stretching vibrations of –OH, C=O, skeletal vibrations of un-oxidized graphitic domain and C-O-C groups, respectively^{1,2}. After silylation with APTMS, FTIR spectra of A-*f*-GO substantiates the insertion of amino silane chain by demonstrating new peaks at 3219 cm^{-1} and 1575 cm^{-1} which corresponds to N-H stretching vibrations³. On the other hand, intensity of –OH groups was almost absolutely shown to be declined suggesting that nearly all –OH groups are substituted/ functionalized by amino groups. An introduction of two new stretching vibrations of Si-O-Si and Si-O-C observed at 1115 and 1037 cm^{-1} also confirms the potent silylation reaction^{3,4}. Peaks observed at 2929 cm^{-1} and 2860 cm^{-1} attributed to the stretching vibrations of C-H bands⁵. Conversely, carboxyl and epoxy groups remain intact and their peaks are distinctly apparent, hence, it can be said that merely –OH is the site of action when functionalized with amino silane moiety.

After the grafting of ligand, new intense peak is examined at 1622 cm^{-1} corresponding to –C=N group in the FTIR spectrum of L-*f*-GO. Upon insertion of metal ion, the lone pair of electron flows from ligand to metal ion and as a result the peak of –C=N group is migrated to 1613 , 1614 and 1596 cm^{-1} in $CuL-f-GO$, $CoL-f-GO$ and $VOL-f-GO$, respectively. This shifting is

being a sign of co-ordination of azomethine nitrogen to the metal ion⁶. From this it can be concluded that FTIR spectra are in good accordance with successful functionalization of –OH groups with APTMS.

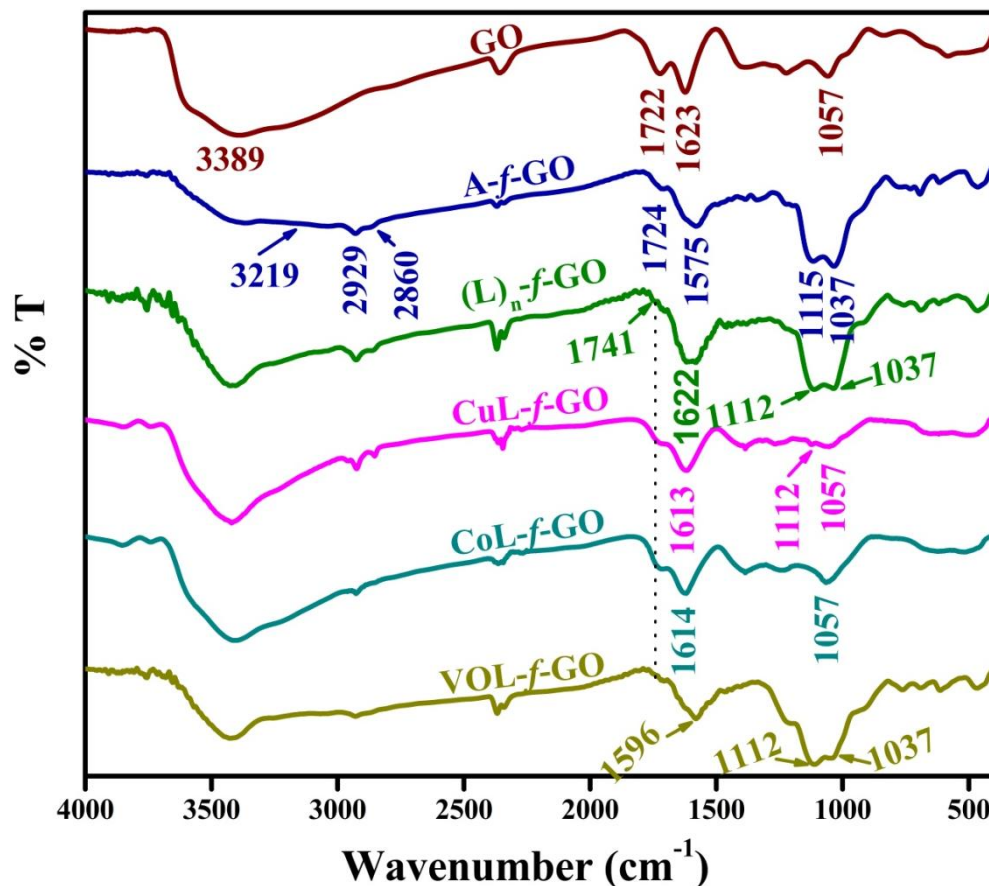


Fig. 3.1. FTIR spectra of GO, A-f-GO, (L)_n-f-GO, CuL-f-GO, CoL-f-GO and VOL-f-GO.

3.1.2. Thermogravimetric analysis

It is very important to inspect the thermal stability of solid heterogeneous catalysts, consequently, TG analysis is performed of as-prepared GO, A-f-GO, CuL-f-GO, CoL-f-GO and VOL-f-GO (Fig. 3.2). TG pattern of GO exhibited typical three stages degradation pattern. First mass loss of 13% is observed in the temperature range of 30 to 150 °C was believed to be of trapped water molecules. The TG curve of GO shows 50% mass loss is examined at 410 °C. 3rd stage mass loss of remaining carbon skeleton is experienced at 600 °C. However, TG curve of A-f-GO exhibits similar pattern to that of GO but differ in percentage mass loss at diverse temperature range.

First mass loss in the temperature range of 30 to 150 °C observed is lower (10.4%) than GO. Whereas 50% mass loss in A-*f*-GO is inspected at 510 °C substantiating the higher degree of functionalization. That means greater amount of oxidative debris, in particular –OH groups, reacted. In contrast to this, thermal degradation pattern of catalysts (CuL-*f*-GO, CoL-*f*-GO and VOL-*f*-GO) demonstrates dissimilar two stage mass loss. All these catalysts, in the first stage, losses trapped water molecules within the temperature range of 30-140 °C and gave mass loss of 8.36%, 8.11% and 9%, respectively. The second stage shows massive loss due to concurrent debasement of carbon skeleton and grafted ligand moiety. Calculated mass losses for this second stage are 76.91%, 80.98% and 77.60% for CuL-*f*-GO, CoL-*f*-GO and VOL-*f*-GO, respectively. Remaining mass percentage is thought to be due to non-degraded metal oxide.

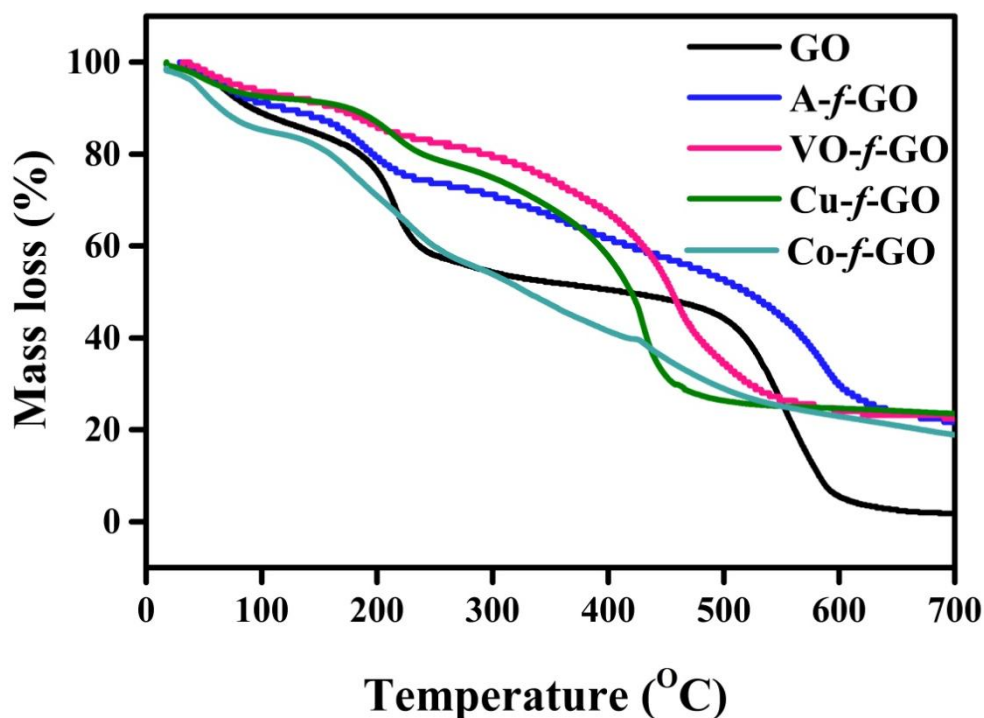


Fig. 3.2. TGA analysis of GO, A-*f*-GO, CuL-*f*-GO, CoL-*f*-GO and VOL-*f*-GO.

3.1.3. UV/Vis. spectroscopy

UV-Visible spectra of GO, A-*f*-GO, VOL-*f*-GO, CoL-*f*-GO and CuL-*f*-GO are depicted in Fig. 3.3. In the UV spectra of GO, the characteristic peak, comparable to literature data, is inspected in the range of 200 – 300 nm⁷. The $\pi \rightarrow \pi^*$ transition of aromatic C=C bond has resulted in the arisen of

absorption peak at about 230 nm, whereas, $n \rightarrow \pi^*$ transition of conjugated aromatic C=O bond has resulted in a shoulder at about 300 nm⁸. This result supports FTIR analysis on the presence of oxidative debris onto the surface of GO nanosheet. However, electronic spectrum of A-*f*-GO exhibits blue shifting of the peak at 230 nm in GO and re-located at 215 nm. This down-shifting of ~15 nm might be due to the formation of more sp^2 carbon which gives rise to increase of π -electrons concentration indicating the covalent bonding between amino groups of APTMS and GO nanosheet. In contrast to this, inserting organic functional groups attached covalently and causes reduction in π -electrons density and formation of sp^3 carbon which causes structural arrangement that can be clearly apparent from the gradually increasing intensity of the shoulder with functionalization⁹. Moreover, the peak at 230 nm in GO is further experiences blue shift on modification by Schiff base ligand and the metal ions while the peak at 300 nm demonstrates red shift might be due to increasing concentration of C=O. This red shift validates the successful attachment of Schiff base ligand and the metal ion to the GO.

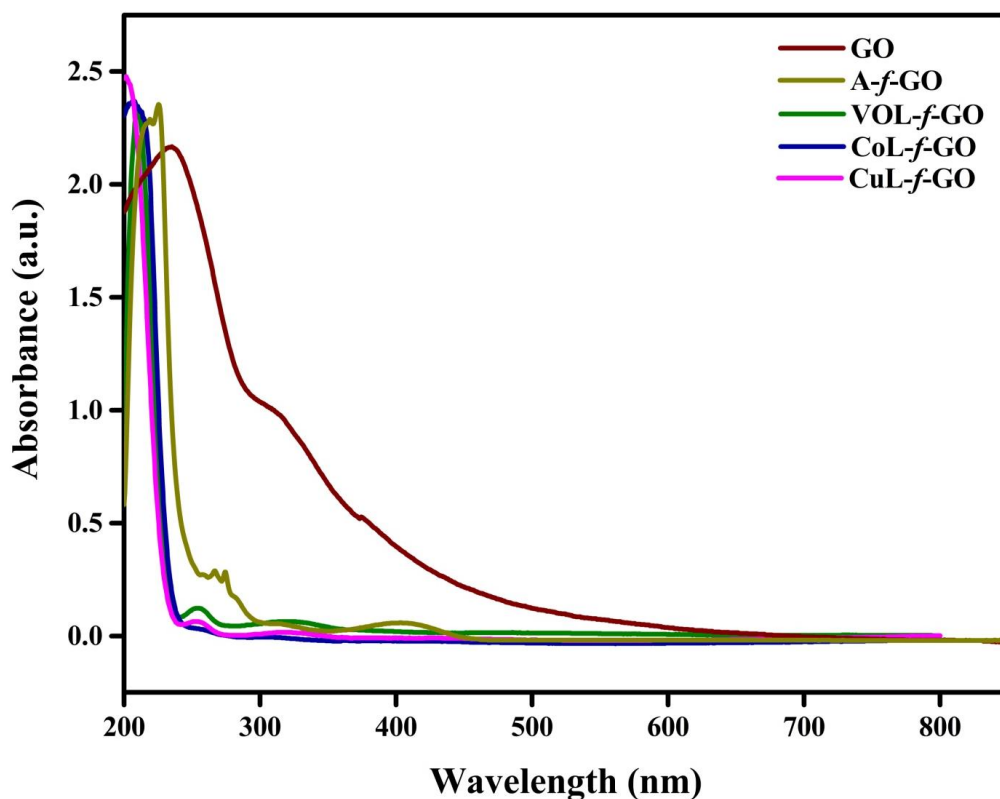


Fig. 3.3. UV/Vis spectra of GO, A-*f*-GO, VOL-*f*-GO, CoL-*f*-GO and CuL-*f*-GO.

3.1.4. Raman spectroscopy

Raman spectroscopy; named after the Indian physicist C. V. Raman is a non-destructive spectroscopic technique classically used to characterize materials to be acquainted with detailed information regarding chemical and structural fingerprint, crystallinity and molecular interactions. As vibrational frequencies are definite to a molecule's chemical bonds and symmetry Raman gives a distinctive fingerprint. For graphitic material particularly, D and G bands as well as their overtone are the typical characteristics of Raman spectroscopy. In the Raman spectra of GO (Fig. 3.4) these D and G bands are found at 1334 and 1578 cm^{-1} corresponding to the out of plane vibrations of breathing mode/ defects of graphitic ring due to the presence of defects and in-plane vibrations of E_{2g} phonon of sp^2 bonded carbon atoms in rings and chains¹⁰, respectively.

The degree of defects in the as-prepared samples can be estimated through calculating the intensity ratio of D/G band. Here, ID/IG ratio for GO is found to be 0.84 and it showed increasing trend on functionalization and grafting with amino silane moiety (APTMS), ligand as well as metal ion, respectively. For A-*f*-GO, it is observed to be 1.01; whereas for CuL-*f*-GO, CoL-*f*-GO and VOL-*f*-GO it is found to be 1.04, 1.04 and 0.9, respectively. This increase in ID/IG ratio is due to rise in disorder due to formation of sp^3 carbon suggesting successful functionalization with APTMS moiety, Schiff base ligand and the metal ion¹¹. This functionalization and grafting also reflects as up-shifting of G band in the Raman spectra of A-*f*-GO, CuL-*f*-GO, CoL-*f*-GO and VOL-*f*-GO. This red shift likely to be owing to effective charge transfer from GO to amino-silane moiety as well as the metal ion causing strain due to covalent attachment^{12,13}. This increase in intensity ratio and defects points towards little increase in amorphous nature due to losing the hydrophilicity of GO¹⁴. This data are in good accordance with XRD and HRTEM results.

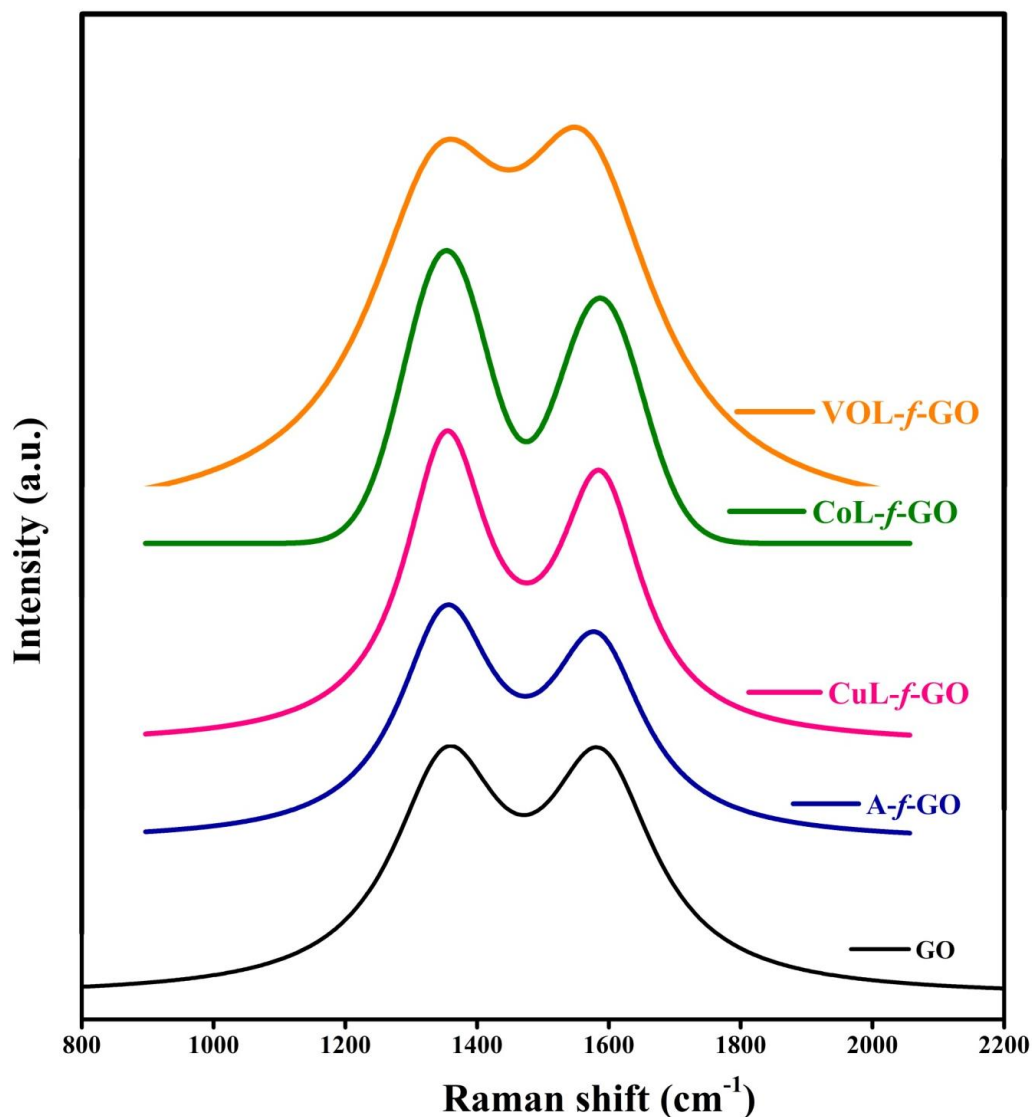


Fig. 3.4. Raman spectra of GO, A-*f*-GO, CuL-*f*-GO, CoL-*f*-GO and VOL-*f*-GO.

3.1.5. XRD patterns

XRD analysis is crucial spectroscopic tool to explore the crystallinity of synthesized materials. Fig. 3.5 demonstrates the XRD patterns of GO, A-*f*-GO, CuL-*f*-GO, CoL-*f*-GO and VOL-*f*-GO. In the XRD pattern of GO, a strong characteristic diffraction peak of the crystal plane is observed at $2\theta = 11.2^\circ$ substantiated high degree of oxidation of graphite to GO¹⁵. It is well known that pristine graphite demonstrates a characteristic peak at $2\theta = 26.5^\circ$ with an interlayer distance of 3.36 Å. However, this interlayer distance, after oxidation, increases to 8.1 Å (calculated using Bragg's equation) in GO due to introduction of oxidative functional groups on basal plane and edges of each

layer¹³. One more characteristic peak observed in graphitic materials at $2\theta = 42.2^\circ$ is might be due to the defects caused by residual trace MnO_2 , produced during synthesis, in the un-exfoliated GO sheets. In the XRD pattern of A-*f*-GO, intensity of the peak at $2\theta = 10.9^\circ$ in GO, is experienced noteworthy shortfall due to abolishment of hydroxyl groups from the surface of GO indicating the successful transformation into amino groups. However, this peak is not vanished absolutely that confirms the retention of other oxidative debris and these findings are consistent with FTIR and XPS spectra. Except increase in roughness due to loss of hydrophilicity, XRD pattern of A-*f*-GO demonstrates characteristic peaks similar to GO revealing that integration of amino-silane moiety do no alter the hexagonal two dimensional property of GO.

However, in the XRD spectra of $\text{M(L)}_n\text{-}f\text{-GO}$ ($\text{M} = \text{VO}^{4+}, \text{Co}^{2+}, \text{Cu}^{2+}$), the peak centred at around $2\theta = 26.5^\circ$ in the XRD spectra of GO and A-*f*-GO is migrated to lower 2θ value. This blue shift is believed to be due to more disordered layers of GO nanosheets¹⁵. Moreover, it is probable to calculate the approximate nanocrystallite size from XRD data¹⁶ through Debye-Scherrer equation. We have calculated the size of as-prepared ML-*f*-GO catalyst assuming the spherical shape of crystallite. The estimated size for VOL-*f*-GO, CoL-*f*-GO and CuL-*f*-GO is 3.08, 2.48 and 2.6 nm, respectively. This calculated approximate size is analogous to the size calculated by Image J software from HRTEM result (7-13 nm).

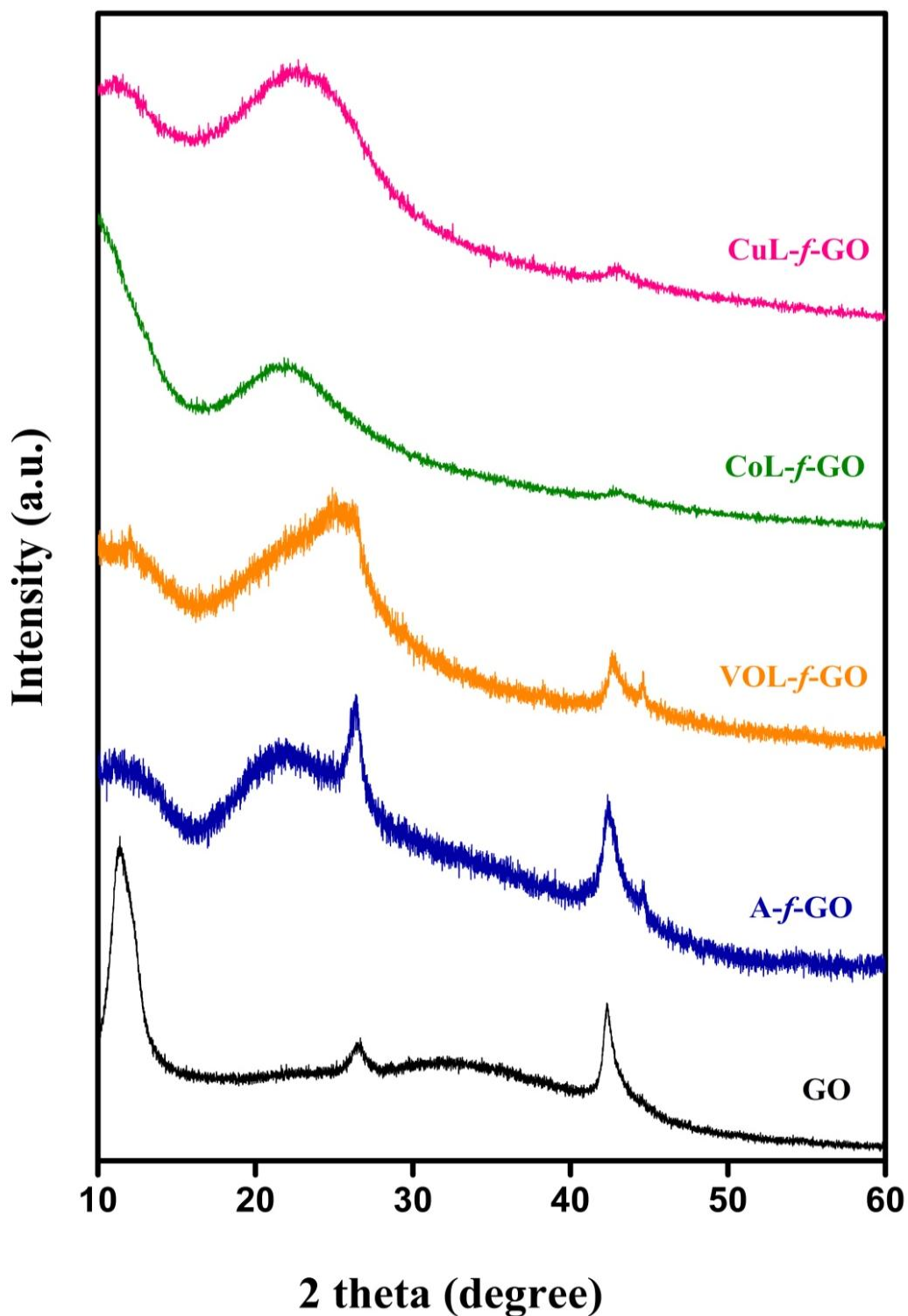


Fig. 3.5. XRD pattern of GO, A-*f*-GO, VOL-*f*-GO, CoL-*f*-GO and CuL-*f*-GO.

3.1.6. XPS analysis

Furthermore, elemental constitution and bonding environment of the as-prepared catalysts is estimated through XPS analysis. Fig. 3.6 shows the full range XPS survey spectra of GO, A-*f*-GO, VOL-*f*-GO, CoL-*f*-GO and

CuL-*f*-GO. It reveals that GO is consist of merely C and O elements exhibiting characteristic signals at 286.1 and 533.3 eV, while after *in situ* silylation with APTMS, the presence of N and Si elements are also documented in the XPS survey spectra of A-*f*-GO. A peak at 400.2 eV is attributed to N1S and second peak at 101.4 eV is emerged in the form of Si 2p spectrum¹⁶ corroborating successful insertion of amino-silane moiety to the GO surface. However, presence of metal ion is confirmed by emerging peaks at different binding energy, for instance, peak at 531.2, 780.6 and 933.5 eV is correspond to VO 2P, Co 2P and Cu 2P metal, respectively. This data confirms the successful grafting of ligand and metal complexes.

Moreover, high-resolution C1S spectra (Fig. 3.7A, 3.8A, 3.9A, 3.10A and 3.11A) demonstrates the bonding structure as C-C, alkoxy C-O, epoxy C-O-C, ester and carboxy C=O observed at 284.5, 286.3, 288.2 and 289.2 eV, respectively in GO; as 284.6, 286.2, 288.2 and 289.1 eV, respectively in A-*f*-GO; as 284.5, 286.1, 288.3 and 289.1 eV, respectively in CuL-*f*-GO; as 284.6, 286.2, 288.2 and 289.1 eV, respectively in CoL-*f*-GO, as 284.6, 286.1, 288.1 and 289.1 eV, respectively in VOL-*f*-GO signifying successful oxidation of graphite by modified Hummers' method. Changes due to insertion of N onto GO sheet are clearly identified in the magnified view of C1S spectra of A-*f*-GO. A peak at 286.3 in C1S spectra of GO is lessened and new peak arises at 286.6 indicating successful covalent attachment of N of amino-silane moiety to the graphene sheet^{17,18}. High resolution N1S spectra of A-*f*-GO also supports this covalent attachment by exhibiting peaks at 398.8, 400.3, 401.03, 402.1 and 403.3 eV which corresponds to C-N originating from miscellaneous -C-N bonds (viz. >C=N, -C-NH₂, -C-N-C, O=C-NH₂, -NH⁺), N-H, N-CO, NH₂, and Ar-NH₂, respectively. After the thermal reaction with Schiff base ligand and the metal ions, -NH bond converts to N=C due to the donor-acceptor interaction between N and central metal ions¹⁹. High resolution O1S spectra of GO fitted into four peaks at 530.5, 531.5, 532.1 and 533.5 eV which are attributed to quinines, C=O (carbonyl and carboxyl), C-O (epoxy and hydroxyl) and -OH, respectively. Whereas, magnified view of O1S spectra of A-*f*-GO (Fig. 3.7B) demonstrates a new peak at 534.1 eV due to absorbed water within and near the surface of sample^{17,20}. However, removal of -OH confirms the functionalization of -OH groups by APTMS.

The bonding energy of Cu, Co and VO metal ions is reflected in Fig. 3.9D, 3.10D and 3.11 D, respectively. The “shake-up” satellite peaks at 941.8 and 962.1 eV in the Cu 2p XPS spectrum (Fig. 3.9D) authenticates the existence of Cu^{2+21,22}. In addition to this, two distinct peaks at 933.5 and 952.8 eV are attributed to Cu 2p_{3/2} and Cu 2p_{1/2}, respectively. This spin-orbit-coupled Cu2p region substantiates the presence of Cu^{1+23, 24}. However, high resolution Co2p spectra (Fig. 3.10D) exhibits two contributions at 780.5 and 796.3 eV, arising from Co2p_{3/2} and Co2p_{1/2}, respectively. Additional peaks at 786.4 and 803.01 eV are ascribed to the “shake up” satellite peak point towards the existence of Co₃O₄²⁵. However, for VO, peaks observed at 516.1 and 523.01 eV are corresponds to VO 2p_{3/2} and VO 2p_{1/2} (Fig. 3.11D) while the O1S peaks are crimped in to two peaks at 529.8 and 532.1 eV. Amongst them, former is considered to vanadium oxide (V=O) and second is owing to hydroxide or carbonate contamination. These results reveal the presence of VO ion as VO₃O₄, Co ion as Co₃O₄ and Cu ion as Cu₂O and CuO. These results are in good agreement with XRD data which also confirms the existence of VO₃O₄, Co₃O₄, Cu₂O and CuO.

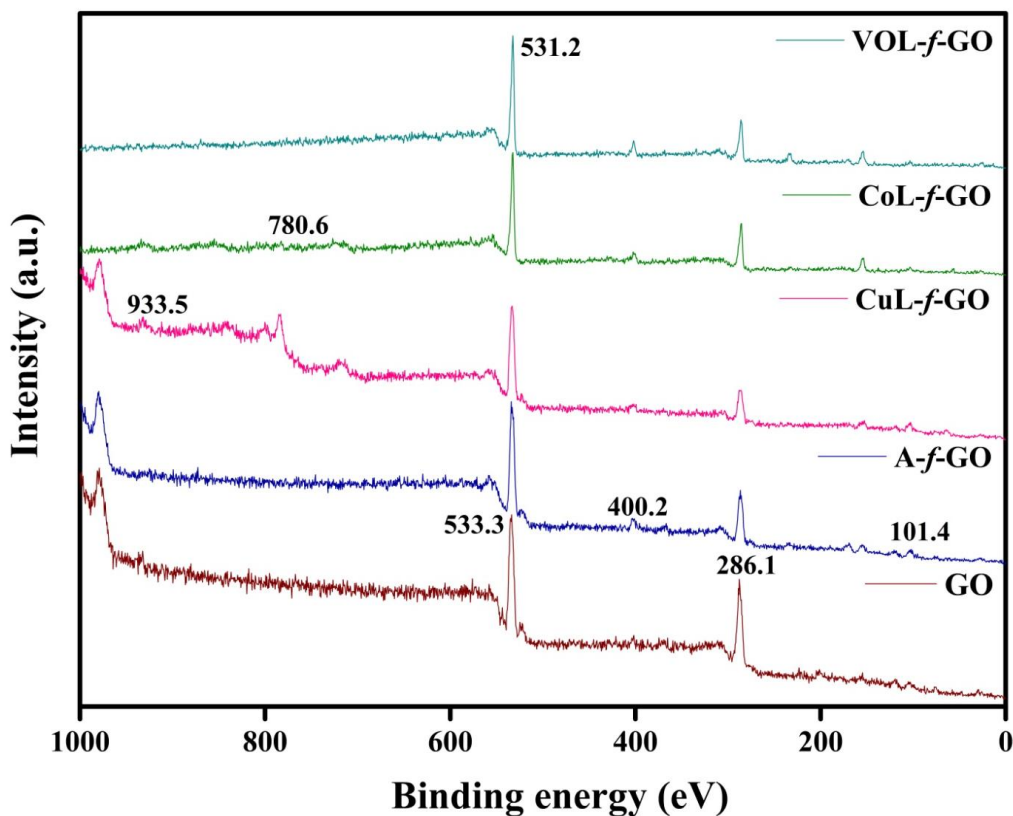


Fig. 3.6. Full range XPS survey spectra of GO, A-*f*-GO, CuL-*f*-GO, CoL-*f*-GO and VOL-*f*-GO.

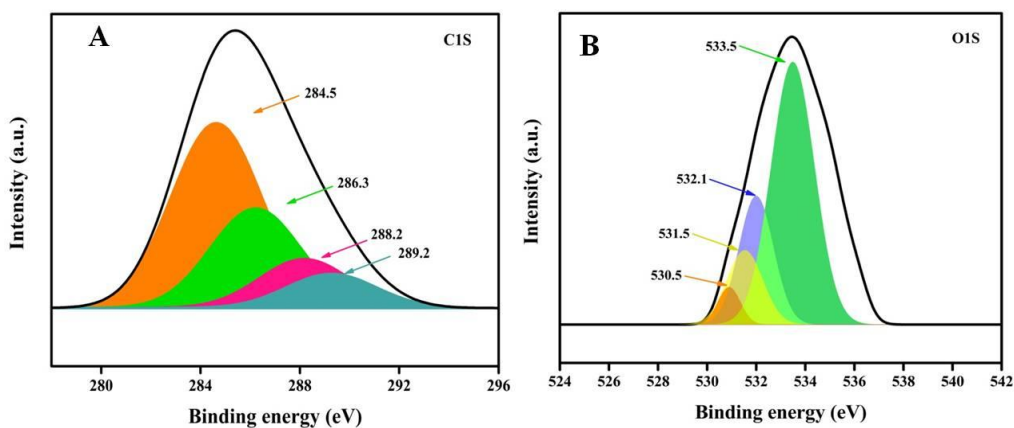


Fig. 3.7. High resolution XPS spectra of GO; (A) C 1S, (B) O 1S.

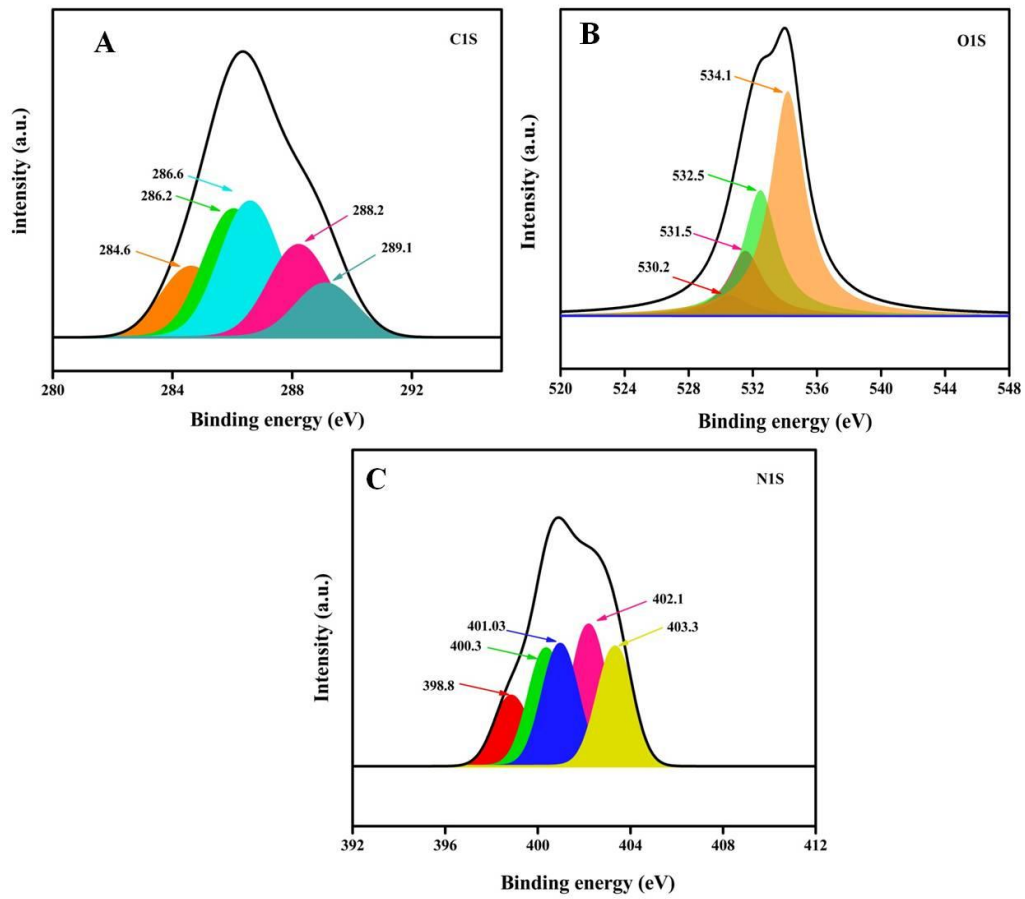


Fig. 3.8. High resolution XPS spectra of A-f-GO; (A) C 1S, (B) O 1S and (C) N 1S.

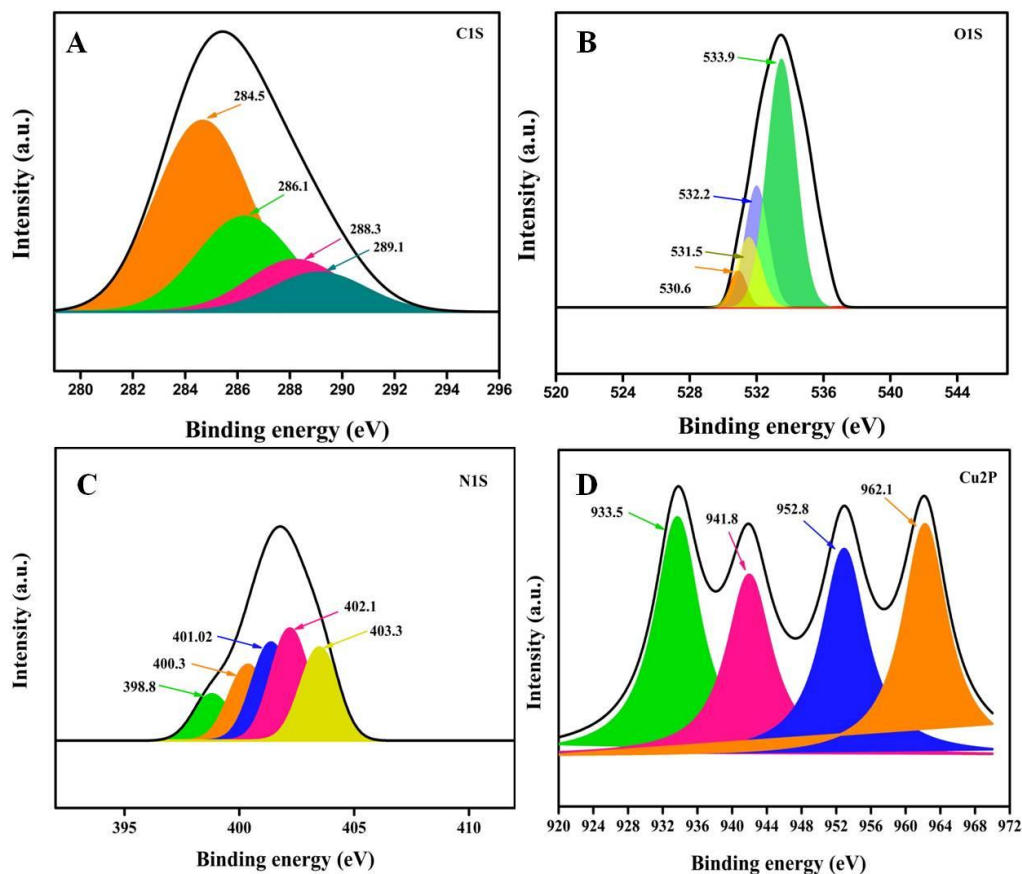


Fig. 3.9. High resolution XPS spectra of CuL-*f*-GO; (A) C 1S, (B) O 1S, (C) N 1S and (D) Cu 2P.

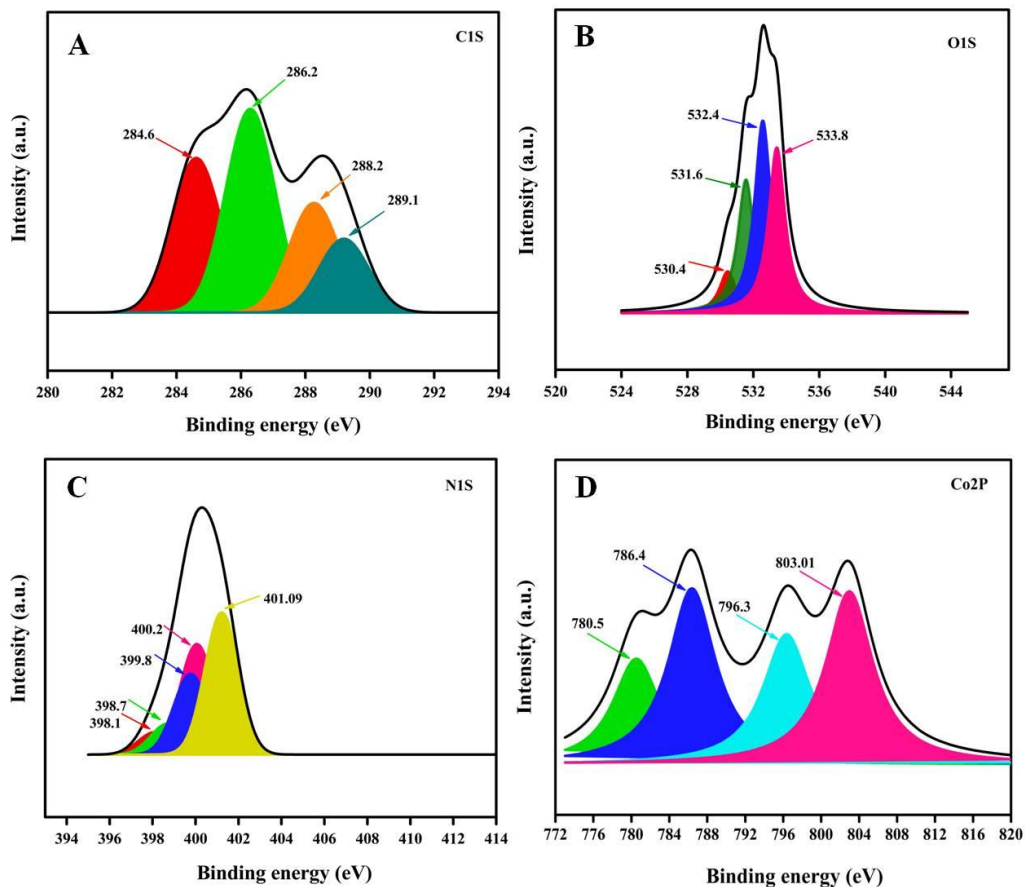


Fig. 3.10. High resolution XPS spectra of CoL-f-GO; (A) C 1S, (B) O 1S, (C) N 1S and (D) Co 2P.

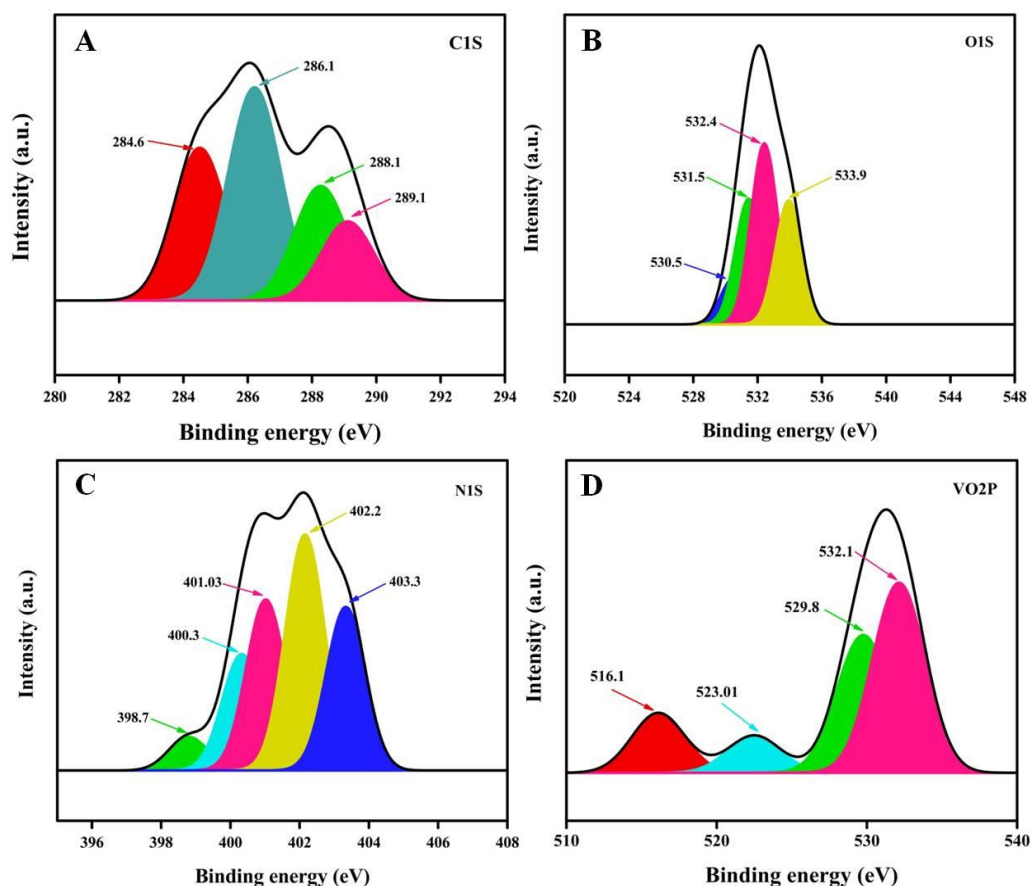


Fig. 3.11. High resolution XPS spectra of VOL-*f*-GO; (A) C 1S, (B) O 1S, (C) N 1S and (D) VO 2P.

3.1.7. HRTEM analysis

To be acquainted with more structural and morphological characteristic features, as-prepared catalysts are examined methodically through HRTEM analysis in association with selected area electron diffraction (SAED) pattern as shown in Fig. 3.12. Two-dimensional sheet-like structure of GO with manifold lamellar layered construction stacked one on other is clearly observed from Fig. 3.12(A). In this stacked arrangement, GO sheets aggregate primarily at the edges results in more thickness of GO sheet at the edges. The reason for this high thickness is believed to be due to the insertion of oxidative functional groups²⁶, since the oxygenated functional groups are mainly unite together by dangling bonds. In addition, after insertion of amino moiety and metal ion, thickness of GO at the edges further increases. A glimpse of the HRTEM images of the samples evidently illustrates that after silylation

reaction with APTMS and grafting with metal ions, GO nanosheet loses hydrophilicity resulting in more roughness of the surface²⁷ which is in harmony with Raman analysis. The black spot in the Fig. 3.12(K, O and S) indicates high metal loading and homogeneous distribution of metal particles.

The selected area electron diffraction (SAED) pattern of GO [Fig. 3.12(D)] reveals diffraction ring with no visible diffraction dots signifying the amorphous nature of the GO nanosheet²⁸. On the other hand, SAED pattern of A-*f*-GO, VOL-*f*-GO, CoL-*f*-GO and CuL-*f*-GO exhibits same blueprint with no visible diffraction dots. This confirms that silylation reaction with APTMS and grafting of metal ions does not alter the materials morphology. This data are in good agreement with XRD results. The average particle size is calculated using Image J software. The particle size for VOL-*f*-GO, CoL-*f*-GO and CuL-*f*-GO is calculated to be 2.7 ± 0.14 , 2.51 ± 0.15 and 2.7 ± 0.3 nm, respectively [Fig. 3.12(U, V and W)]. Hence, from this results we can corroborate the successful insertion of amino-silane moiety and grafting of ligand as well as metal ions. This data also supports the conservation of structural and morphological characteristic of material during synthesis.

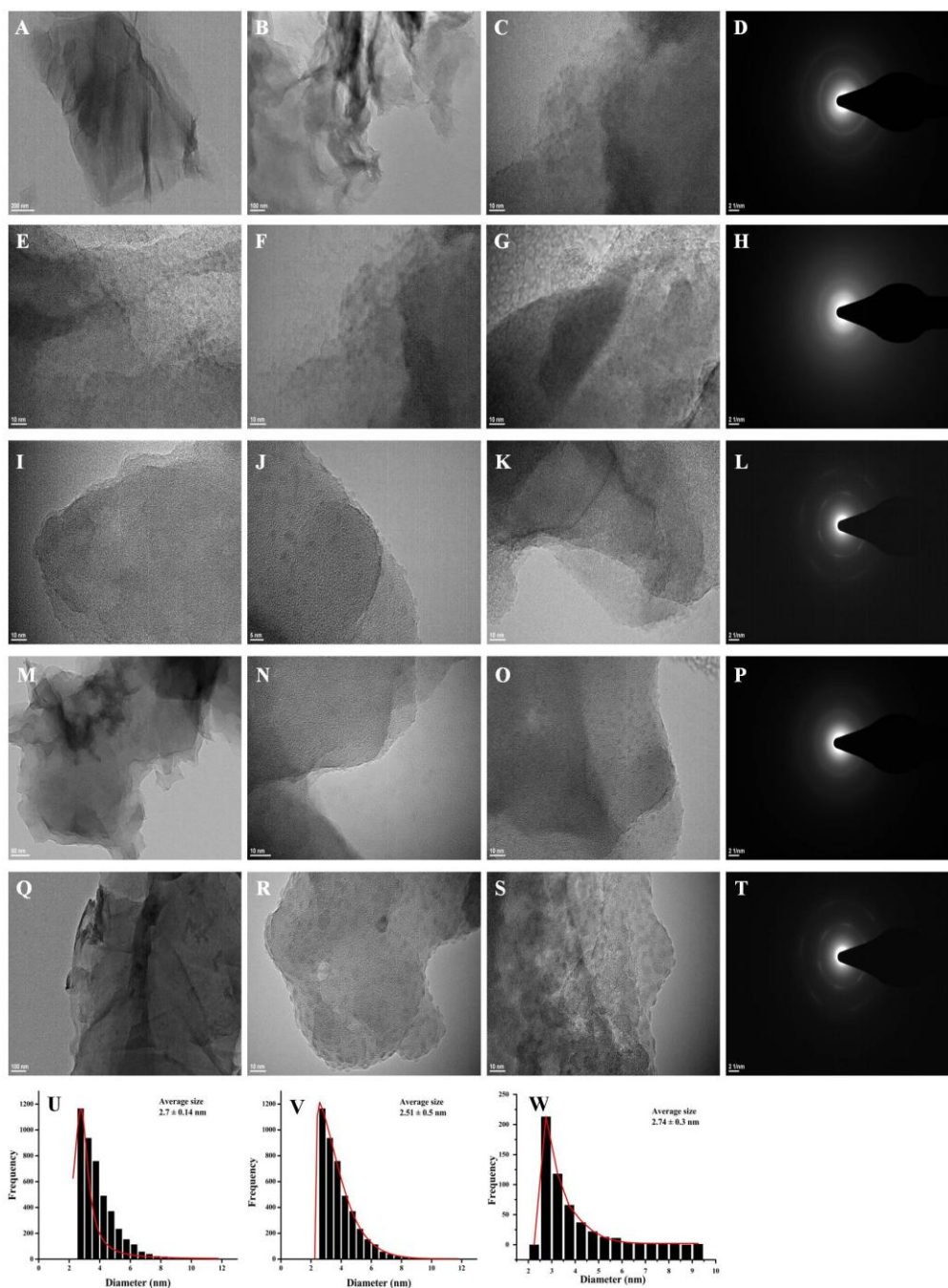


Fig. 3.12. HRTEM images of GO (A-C), A-*f*-GO (E-G), VOL-*f*-GO (I-K), CoL-*f*-GO (M-O), CuL-*f*-GO (Q-S), selected area electron diffraction (SAED) patterns of GO (D), A-*f*-GO (H), VOL-*f*-GO (L), CoL-*f*-GO (P), CuL-*f*-GO (T) and average particle size distribution histograms of VOL-*f*-GO (U), CoL-*f*-GO (V), CuL-*f*-GO (W).

3.1.8. ICP-OES analysis

With the results of ICP-OES analysis, the metal content in as-synthesized catalysts has been estimated as 23.01, 4.456 and 10.736 ppm for V, Co, and Cu, respectively. Metal loading per gram of catalysts is calculated using the formula: [Concentration of metal (ppm or mg/litre) x volume of the extract (litre)] / weight of the solid sample taken for extraction (gram)] to be 46.02, 8.912 and 21.472 mg/g for VOL-*f*-GO, CoL-*f*-GO and CuL-*f*-GO, respectively.

3.1.9. BET analysis

BET analysis makes obvious that as-prepared GO possess 94.23 m²/g of surface area, while after the functionalization with APTMS surface area is reduced to 40.70 m²/g which is further reduced to 33.37 m²/g after the immobilization of Schiff base metal complex.

3.1.10. DFT study

In this functionalization, we have first optimized 42 atoms hydrogen terminated graphene sheet, each of two functional groups i.e. -COOH, -OH, C-O-C and -NH₂ on the graphene sheet. To find the appropriate attachment site for carboxyl group on GO sheet, we have calculated binding energy between carboxyl, epoxy (epoxide), hydroxyl, amine groups and graphene sheet by placing the carboxyl group at numerous sites of the graphene sheet. This calculated binding energy values for diverse sites confirm that the carboxyl groups prefer to bind at the edges [Fig. 3.13(b)] instead of the basal plane which is consistent with the reported works^{29,30}. However, the epoxy or epoxide group has a propensity to locate at the top site of the graphene nanosheet [Fig. 3.13(c)] and changes the hybridization of carbon from sp² to sp³ with a binding energy of -2.078 eV listed in Table 3.1. The hydroxyl and amino groups have a tendency to unite on graphene sheet in zig-zag or arm chair direction of carbon atoms. From these calculations we can conclude that all functional groups except carboxyl group which binds at edges attach to graphene sheet on its basal planes. Moreover, the binding energy calculation demonstrates that the binding energy of the amino group is -1.522 eV which is higher than hydroxyl group i.e. -0.972 eV and lesser than epoxy and carboxyl

groups (Table 3.1), respectively. However, the reactivity of carboxyl and epoxy functional groups towards graphene sheet is higher than that of hydroxyl and amino groups leading to conservation of their site. In other words, the possibility of substitution of carboxyl and epoxy groups by amino groups is negligible. However, as a result of low binding energy, hydroxyl groups show positive response towards the substitution with amino groups. Here, reactivity of amino group and hydroxyl group is found to be almost same, consequently the chances of replacement of hydroxyl groups is higher than that of other functional groups.

The optimized Cu and Co based catalysts viz. CuL-*f*-GO and CoL-*f*-GO, on the graphene sheet are illustrated in Fig. 3.14. Usually, the electronic nature of materials plays a crucial role in understanding the choice of chemical properties, for instance, interaction, chemical stability and/or reactivity. Hence, in order to find the reactivity, recyclability and chemical stability of catalysts, highest occupied molecular orbital (HOMO) and lowest unoccupied molecular orbital (LUMO) (Fig. 3.15) are calculated which has been reported earlier too³¹. The magnitude of HOMO can be recognized as ionization potentials and its high value expresses the high stability and chemical inertness. These two properties are especially vital for any catalyst to prove their potency. From these outcomes (Table 3.2), it is manifestly stated that CuL-*f*-GO will be profitable and of better-quality for its catalytic aptitude. Energy gap, global hardness and softness of considered transition metal-based catalysts are also calculated using Koopman's theorem. Energy gap, global hardness and softness of CuL-*f*-GO and CoL-*f*-GO are also calculated using Koopman's theorem. As said by maximum hardness principal, materials with high value of hardness produce the resistance to the deformation under a small perturbation of chemical reaction. No significance difference is observed in the global hardness and softness value of both transition metal-based catalysts, though Cu immobilized catalyst has shown a better catalytic activity. These results are in good harmony with our experimental results.

Table 3.1

Calculated binding energy of graphene sheet functionalized by different groups along with other available data.

System	Binding energy E_B (eV)
Graphene + OH	-0.972,-1.338 ³²
Graphene + NH ₂	-1.522
Graphene + O	-2.078,-3.809 ³²
Graphene + COOH	-2.10

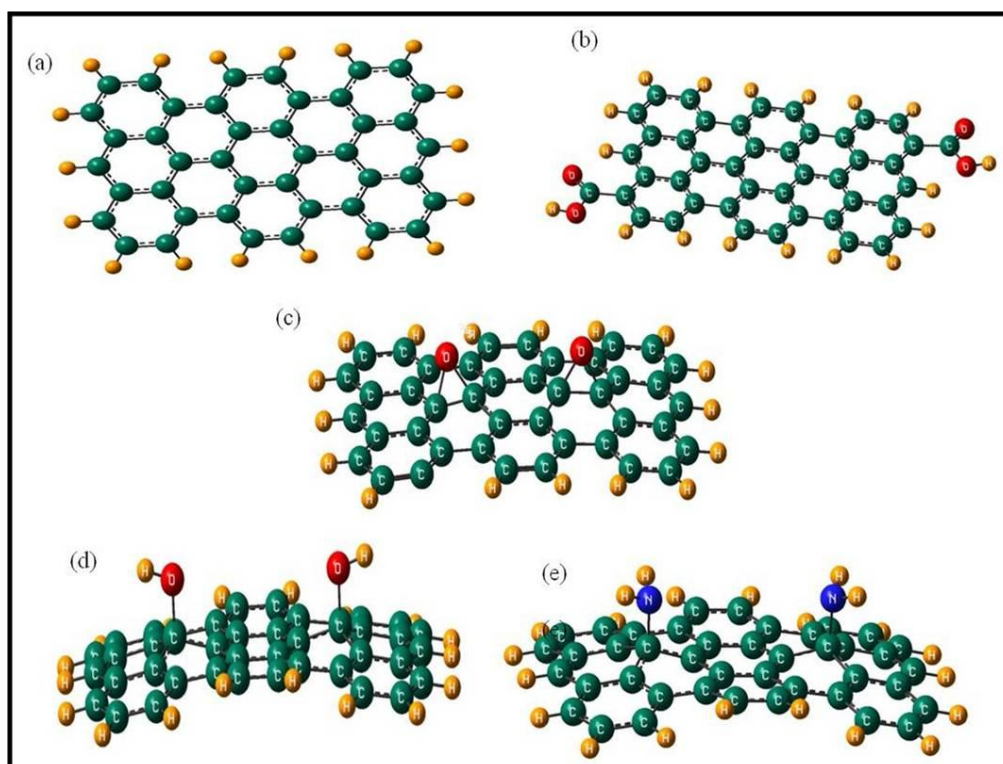
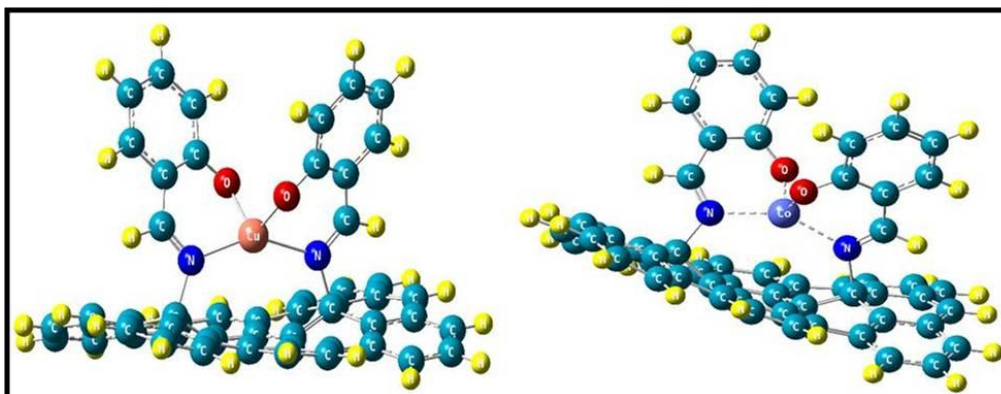


Fig. 3.13. Atomic model for graphene (a), graphene with two carboxylic groups at edge of graphene (b), graphene with two epoxy groups at basal of graphene (c), graphene with two hydroxyl groups at basal of graphene (d) and graphene with two amino groups at basal of graphene (e).

Table 3.2

Calculated HOMO, LUMO, energy gap, global hardness and softness of CuL-*f*-GO and CoL-*f*-GO catalysts.

Catalyst	HOMO (E_H) (eV)	LUMO (E_L) (eV)	ΔE ($E_L - E_H$) (eV)	η ($0.5 \times$ ($E_L - E_H$) (eV))	S ($1/2 \eta$) (1/eV)
CuL- <i>f</i> -GO	-4.7412	-2.6752	2.07	1.04	0.49
CoL- <i>f</i> -GO	-4.6272	-2.5783	2.05	1.03	0.48


Fig. 3.14. An atomic model for CuL-*f*-GO and CoL-*f*-GO.

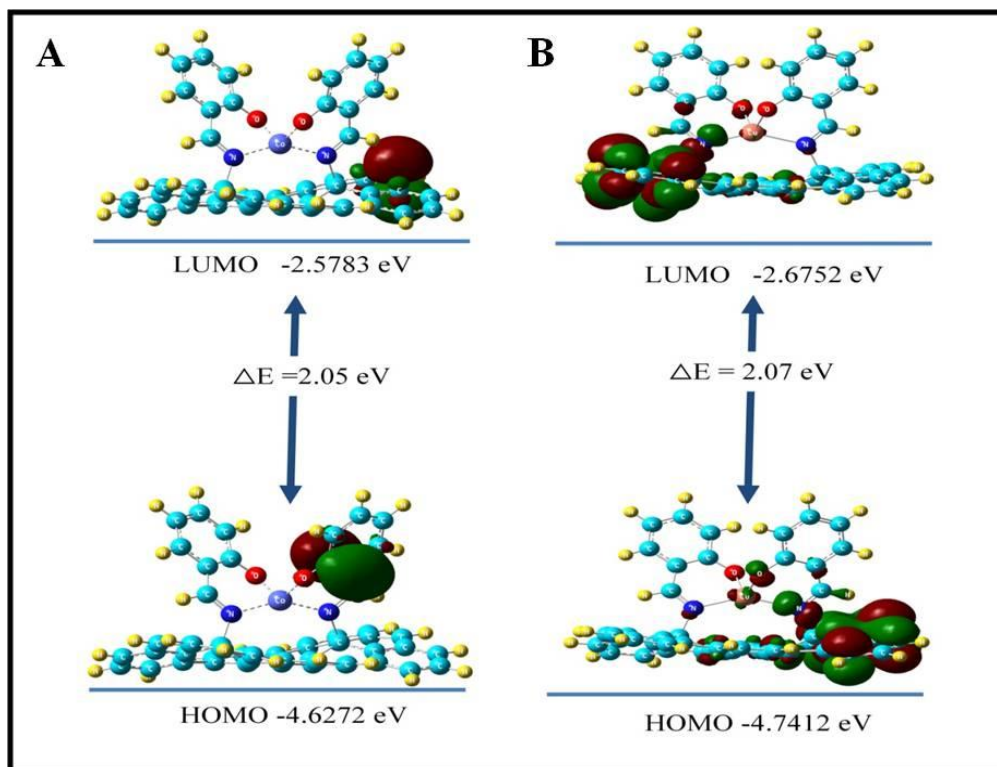


Fig. 3.15. HOMO and LUMO of (A) CoL-*f*-GO and (B) CuL-*f*-GO

3.2. Characterization of –COOH functionalized catalysts

A catalysts synthesized by modifying –OH groups of GO is commonly represented as M(L)-*f*-GO (i.e. Co-*f*-GO, VO-*f*-GO, Cu-*f*-GO).

3.2.1. FTIR analysis

Fig. 3.16 shows the FTIR spectra of GO, Cl-*f*-GO, salen (ligand), neat Co-salen, neat VO-salen, neat Cu-salen, Co-*f*-GO, VO-*f*-GO and Cu-*f*-GO which corroborates the successful oxidation of graphite to GO. Besides this, functionalization of oxidative debris, particularly carboxylic acid groups, with SOCl₂ is also be confirmed by FTIR analysis. FTIR spectrum of GO exhibits characteristic vibrations at 3389 cm⁻¹, 1722 cm⁻¹, 1623 cm⁻¹ and 1057 cm⁻¹ are attributed to stretching vibrations of –OH, C=O, skeletal vibrations of unoxidized graphitic domain and C-O-C groups, respectively^{1,2}. After chlorination with SOCl₂, successful formation of Cl-*f*-GO is substantiated by arising of new peak at 785 cm⁻¹ due to formation of C-Cl bond. However, during this functionalization intensity of –OH groups at 3389 cm⁻¹ is seen to

be decreased suggesting that some of the –OH groups is also substituted by chloro groups of SOCl_2 . Theoretical results also corroborate this fact as binding energy of SOCl_2 is comparable with –OH and –COOH groups. Hence, it may probable that SOCl_2 can concurrently functionalized –OH groups also. On the other hand, conservation of C-O-C groups on the surface of GO is verified by FTIR spectrum of Cl-*f*-GO. Moreover, peak at 1623 cm^{-1} is seen to be shifted to 1642 cm^{-1} in the FTIR spectrum of Cl-*f*-GO indicating the formation of –COCl groups³³. This results authenticates the successful reaction took place between GO and chloro groups of SOCl_2 ³³ which also reflects in XRD results.

FTIR spectrum of salen ligands and metal-salen complexes exhibit various bands and majority of IR spectra are coalesced, so in order to have fruitful conversation, only key contribution are discussed. Peaks at 460, 622 and 580 cm^{-1} in the FTIR spectra of neat Co-salen, VO-salen and Cu-salen complexes, respectively, are attributed to $\nu(\text{M-O})$ of metal-oxygen bond. However, peaks appear between $1020\text{--}1280\text{ cm}^{-1}$ are believed to be due to the aliphatic N. Whereas, strong peak at 1635 cm^{-1} is originated from $\nu\text{C}=\text{N}$ vibrations. Peaks seen in the range of $1450\text{ to }1581\text{ cm}^{-1}$ are ascribed to the C=C absorptions³⁴. On the other hand, peak at 3500 cm^{-1} in the FTIR spectrum of salen ligand is found to be declining in the FTIR spectra of metal-salen complexes supports the participation of phenolic oxygen in metal coordination^{35,36}. In addition to this, bands at 622 and 568 cm^{-1} in the FTIR spectra of metal-salen complexes are due to coordination of the metal ions with phenolic oxygen (M–O) and azomethine nitrogen (M–N), respectively³⁵. However, after grafting of metal-slaen complexes (Co/VO/Cu-salen) onto the Cl-*f*-GO, C-Cl peak is disappeared indicating successful grafting of metal-salen complexes.

All the characteristic bands are clearly visible in the FTIR spectra of catalysts with more or less intensity suggesting slight alteration in the morphology of samples and this result is in good accordance with XRD and HRTEM analysis. It is well known that graphene oxide layers are also linked on the edges³⁷⁻⁴⁰ and the rupture edges result in well-packed stacked layers³⁷. This data are in good agreement with XRD results in which after

functionalization with SOCl_2 , inter-planar distance decreases showing well-packed arrangement of GO sheet.

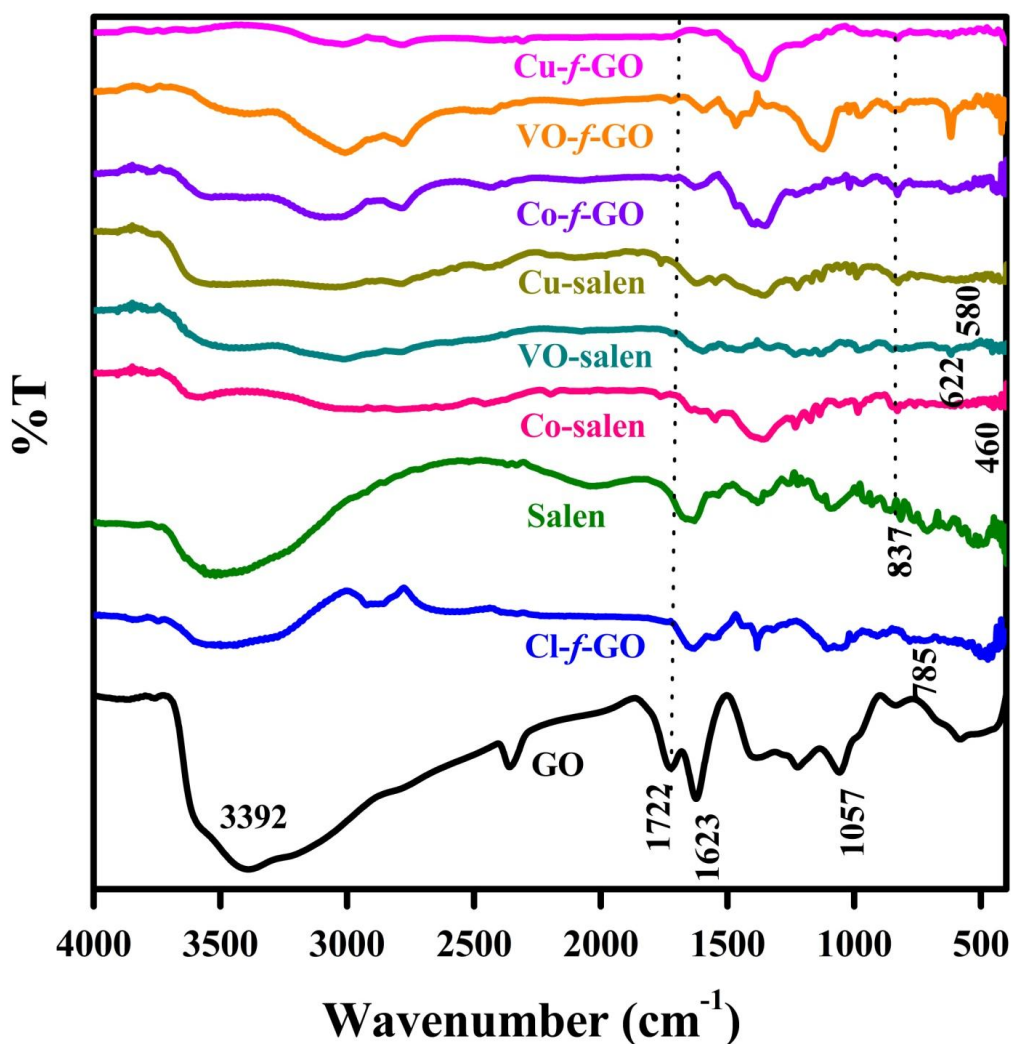


Fig. 3.16. FTIR spectra of GO, Cl-f-GO, salen, neat Co-salen, neat VO-salen, neat Cu-salen, Co-f-GO, VO-f-GO and Cu-f-GO.

3.2.2. Thermogravimetric analysis

TG analysis of as-prepared GO, Cl-f-GO, Salen, Co-salen, VO-salen, Cu-salen, Co-f-GO, VO-f-GO and Cu-f-GO is carried out to study the thermal stability and portrayed in Fig. 3.17. GO demonstrates distinctive three steps degradation model. First mass loss due to trapped water molecule is noticed to be of 13% in the temperature range of 30 to 150 °C. However, 50% mass loss of the whole mass is inspected at 410 °C. Remaining mass loss of residual carbon skeleton is experienced at 600 °C in the 3rd stage. For Cl-f-GO,

similar pattern to that of GO with deviating percentage mass loss in respective temperature range is observed. First mass loss experienced is 10.4% which is less than noticed in GO, while 50% mass loss in Cl-*f*-GO is inspected at 232 °C demonstrating the successful larger degree of functionalization. The reason for this early weight loss is might be the poor physical and chemical stability of COCl groups besides having lack of ability to form H-bond. Another supposed reason for this early weight loss may be that Cl-*f*-GO possesses a lesser amount of oxidative debris onto the surface than that of GO. It signifies that greater amount of –COOH with numerous –OH groups reacted.

However, TG curve of salen ligand shows two stages mass loss pattern. As can be seen, all the metal-salen complexes show almost similar TG pattern to that of salen ligand except in residual metal oxides. The TG inspection of metal-salen complexes at a glance reveals the unlike tendency of metals to react with salen ligand. It gives an idea about the trending of metal loading as VO > Co > Cu which is in good agreement with ICP-OES results.

Contrary to this, in the TG curve of Co-*f*-GO, 50% mass loss is observed at 245 °C indicating successful grafting of Co-salen complex onto the Cl-*f*-GO nanosheet. However, there is not an exaggeration in thinking of weaker attachment of Co-salen which is also experienced in the catalytic results. For VO-*f*-GO, this temperature is increased to 370 °C suggesting somewhat strong attachment of VO-salen to the Cl-*f*-GO nanosheet. Higher degree of attachment can be seen into Cu-salen complex. 3rd stage of mass loss is believed to be due to carbon skeleton. Total mass loss of these three stages in Co-*f*-GO is 87.96%, in VO-*f*-GO it is 80.31% and in Cu-*f*-GO is calculated to be 76.91% and the remaining mass loss of 12.03, 19.68 and 24.94% for Co-*f*-GO, VO-*f*-GO and Cu-*f*-GO, respectively, is considered to be due to non-degraded metal oxide.

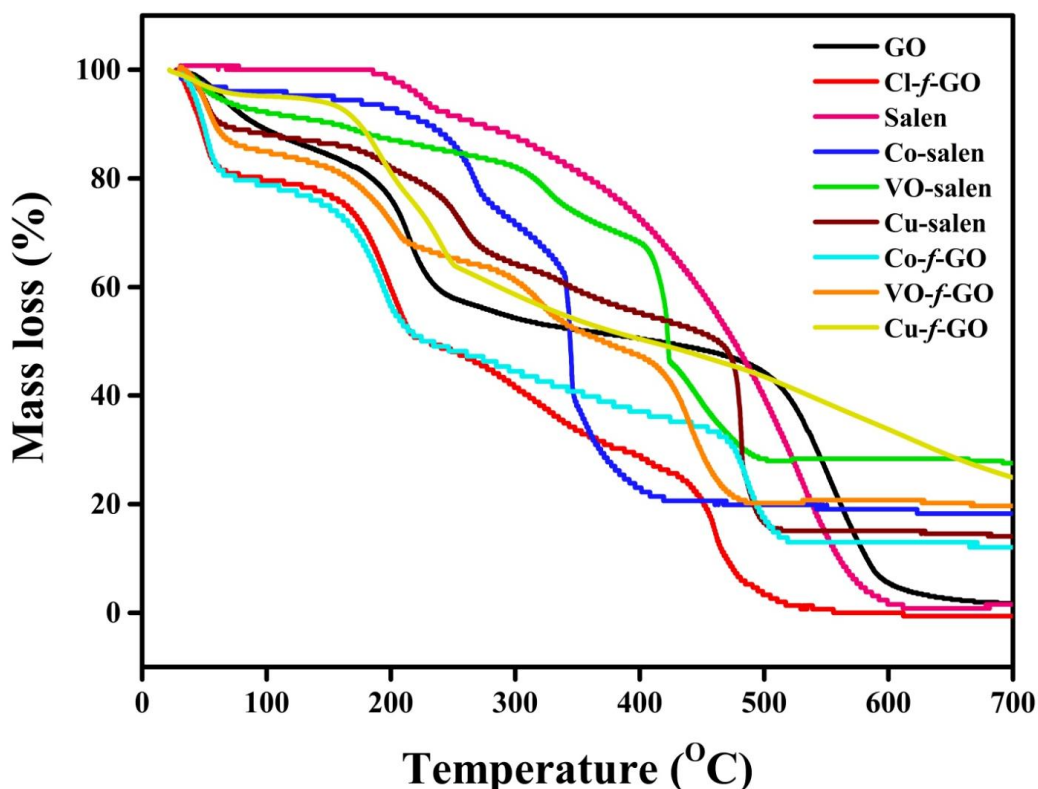


Fig. 3.17. TGA analysis of GO, Cl-*f*-GO, salen, neat Co-salen, neat VO-salen, neat Cu-salen, Co-*f*-GO, VO-*f*-GO and Cu-*f*-GO.

3.2.3. UV/Vis. spectroscopy

UV/Visible absorption spectra of GO, Cl-*f*-GO, salen, neat Co-salen, neat VO-salen, neat Cu-salen, Co-*f*-GO, VO-*f*-GO and Cu-*f*-GO are represented in Fig. 3.18. In the UV spectrum of GO, the distinctive characteristic peak is examined in the range of 200 – 300 nm attributed to $\pi \rightarrow \pi^*$ transition of aromatic C=C bond, and $n \rightarrow \pi^*$ transition of conjugated aromatic C=O bond, respectively^{7,8}. This is in good agreement with the FTIR analysis. Electronic spectrum of salen ligand exhibits two bands below 400 nm are ascribed to intra-ligand charge transfer; $\pi \rightarrow \pi^*$ transition of phenyl rings and $n \rightarrow \pi^*$ transition of –C=N– and –C=O– moieties^{41, 42}. However, weak bands observed in visible region in the metal-salen complexes are believed to be due to d-d transitions⁴³. The electronic spectra of Co-*f*-GO shows strong peaks at around 280 and 323 nm while VO-*f*-GO exhibits at around 275 and 309 nm and Cu-*f*-GO demonstrated at around 285 and 336 nm which are attributed to $\pi \rightarrow \pi^*$ transition of ligand and ligand to metal charge transfer

(LMCT) from phenolic O to metal centre, respectively⁴⁴. All this data and red shifting of the peak of intra-ligand charge transfer confirms the successful functionalization with SOCl_2 and grafting of metal-salen complexes onto Cl-*f*-GO.

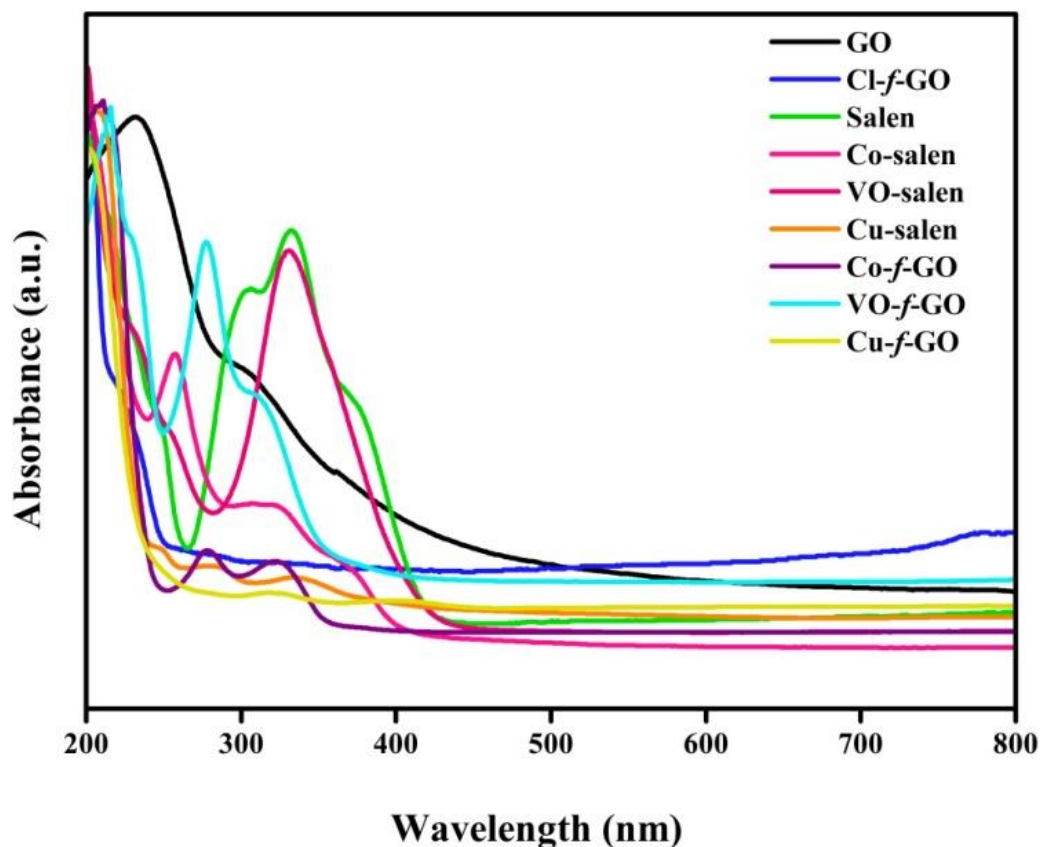


Fig. 3.18. UV/Vis spectra of GO, Cl-*f*-GO, salen, neat Co-salen, neat VO-salen, neat Cu-salen, Co-*f*-GO, VO-*f*-GO and Cu-*f*-GO.

3.2.4. Raman Spectroscopy

Raman spectra of GO, Cl-*f*-GO, Co-*f*-GO, VO-*f*-GO and Cu-*f*-GO are illustrated in Fig. 3.19. In the Raman spectrum of GO, two bands found at 1334 and 1578 cm^{-1} are attributed to out of plane vibrations of breathing mode/ defects of graphitic ring due to the presence of defects and in-plane vibrations of E_{2g} phonon of sp^2 bonded carbon atoms in rings and chains⁴⁵, respectively.

Calculation of intensity ratio of D/G band is usually associated with degree of defects onto the graphitic domain. Here, I_D/I_G ratio for GO is found

to be 0.84, however, it increases to 1.04 in Cl-*f*-GO. This increase in defect clearly points to the formation of sp^3 carbon signifying the successful functionalization with $SOCl_2$. The Raman spectrum of Co-*f*-GO, VO-*f*-GO and Cu-*f*-GO exhibits typical D band at 1389, 1375 and 1360 cm^{-1} , respectively, whereas, G band at 1557, 1557 and 1569 cm^{-1} , respectively. Here, intensity of D and G band is seen to be decline in all catalysts in comparison to Cl-*f*-GO which suggest the reduction in defects (sp^2 carbon). This result suggests that some of the hydroxyl groups adorning the basal plane might be substituted by $SOCl_2$ which is in good agreement with FTIR and XRD results by demonstrating significant declination in the intensity of $-OH$ groups and by decreasing the inter-planar distance, respectively. Moreover, intensity ratio of D and G band in the catalyst is found to be 0.88, 0.98 and 0.99 for Co-*f*-GO, VO-*f*-GO and Cu-*f*-GO, respectively. This decrease in intensity ratio is a sign of reduced amount of amorphous nature/ polycrystalline nature of the catalysts. These data are in harmony with XRD and HRTEM analysis which again confirms polycrystalline nature of metal-salen complexes and decrease in amorphicity in catalyst after grafting of metal-salen complexes.

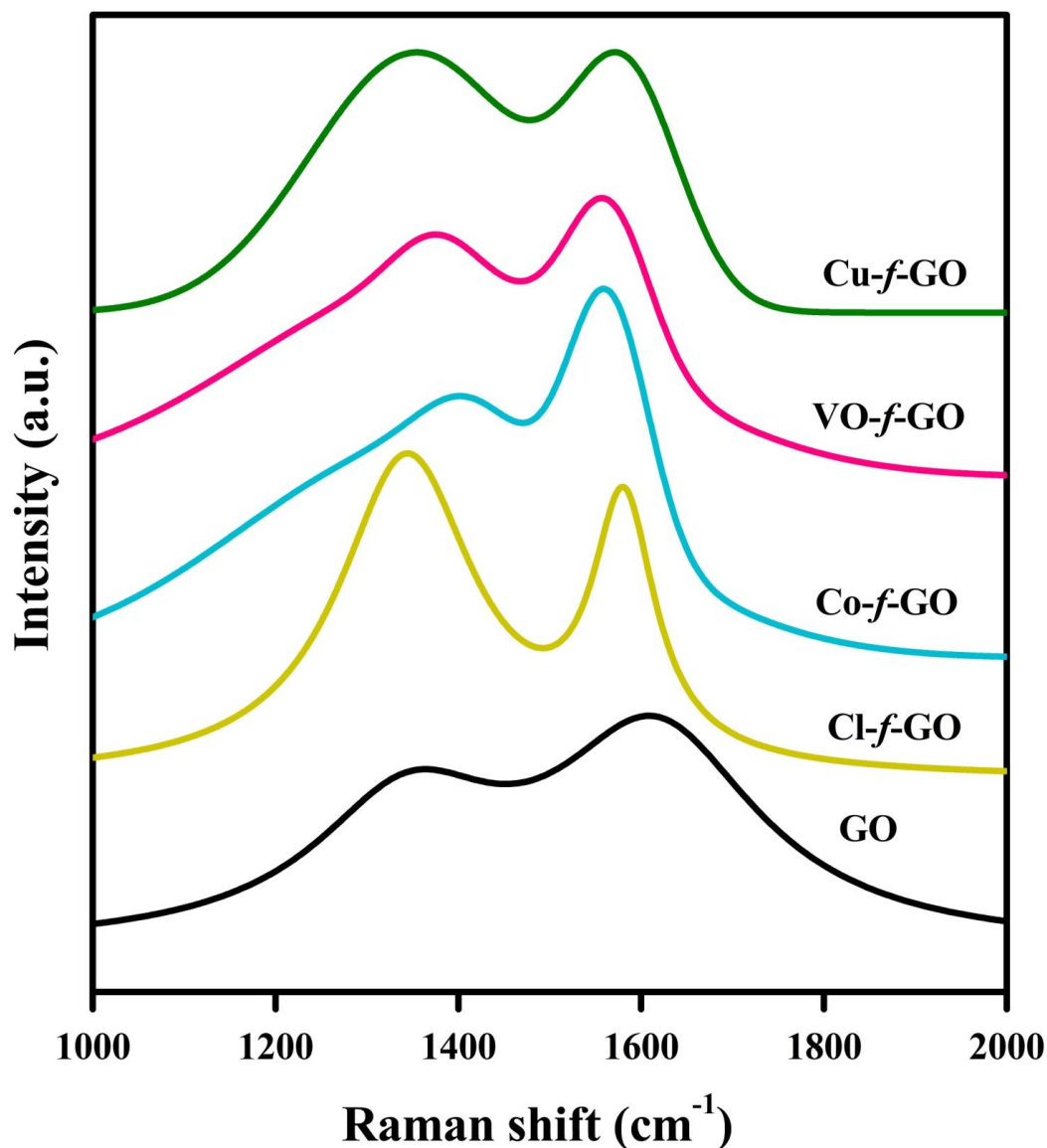


Fig. 3.19. Raman spectra of GO, Cl-*f*-GO, Co-*f*-GO, VO-*f*-GO and Cu-*f*-GO.

3.2.5. XRD patterns

Fig. 3.20 demonstrates the XRD patterns of GO, Cl-*f*-GO, salen, Co-salen, VO-salen, Cu-salen, Co-*f*-GO, VO-*f*-GO and Cu-*f*-GO. In the XRD pattern of GO, characteristic peak of graphite at $2\theta = 26.5^\circ$ weakens to a great extent and a new sharp peak is detected at $2\theta = 11.2^\circ$ being an evidence for high degree of oxidation of graphite to GO by modified Hummers' method⁴⁶. As calculated, inter-planar distance in GO is increased to 8.1 Å that of 3.36 Å in graphite and the reason for this augmentation is considered to be the oxidative debris inserted on the surface during oxidation¹³. XRD pattern of Cl-*f*-GO exhibits a broad peak at $2\theta = 25.01^\circ$ with layer-by-layer distance of 3.55

Å. This decline in inter-planar distance substantiates the formation of –COCl groups by substituting hydroxyl groups of –COOH at the edges along with some of the hydroxyl groups lying on basal plane and these results are in good accordance with outcome of the FTIR and Raman analysis. This staked packing formation, a result of rupture of edges, with inferior inter-planar distance between the subsequent sheets of chloro-functionalized GO may have influence on the grafting and insertion of metal-salen complexes which results in lowering of exposed active sites and hence, in the catalytic activity. However, in the XRD pattern of catalysts (Co-*f*-GO, VO-*f*-GO and Cu-*f*-GO), the minor diffraction peaks found at around 36.9°, 38.6°, 44.8°, 55.7°, and 59.3° are assigned to indices (311), (222), (400), (422) and (511) for Co-*f*-GO corresponds to presence of Co as Co₃O₄⁴⁷, minor peaks at around 20.2°, 21.6°, 26.1°, 32.3°, 37.1°, 41.9°, 45.2° and 57.9° for VO-*f*-GO attributed to (001), (101), (110), (011), (401), (102), (411) and (221) planes of vanadium oxide⁴⁸, respectively, whereas peaks at around 29.8°, 36.8°, 42.7° and 61.8° corresponds to (110), (111), (200) and (220) planes of Cu₂O⁴⁹, respectively, for Cu-*f*-GO. Besides this, it also demonstrates minor peaks at around 35.7°, 39.9°, 47.8° and 60.9 which are indexed to (002), (111), (202) and (113) planes of CuO, respectively. This suggests the co-existence of Cu as Cu₂O and CuO⁵⁰. This data are analogous to JCPDS card no. 43-1003, 89-0612 and 05-0667 along with JPCDS: 48-1548, for Co-*f*-GO, VO-*f*-GO and Cu-*f*-GO, respectively, which confirms the cubic spinal phase of CoO, orthorhombic structure of VO and crystalline cubic phase of Cu₂O. The bonding structure thus obtained is in good accordance with XPS analysis. On the other hand, on grafting with metal-salen complexes, amorphicity of the Cl-*f*-GO sheet is seen to be decreased indicating poly crystalline nature of metal-salen complexes which can also be validate through HRTEM analysis.

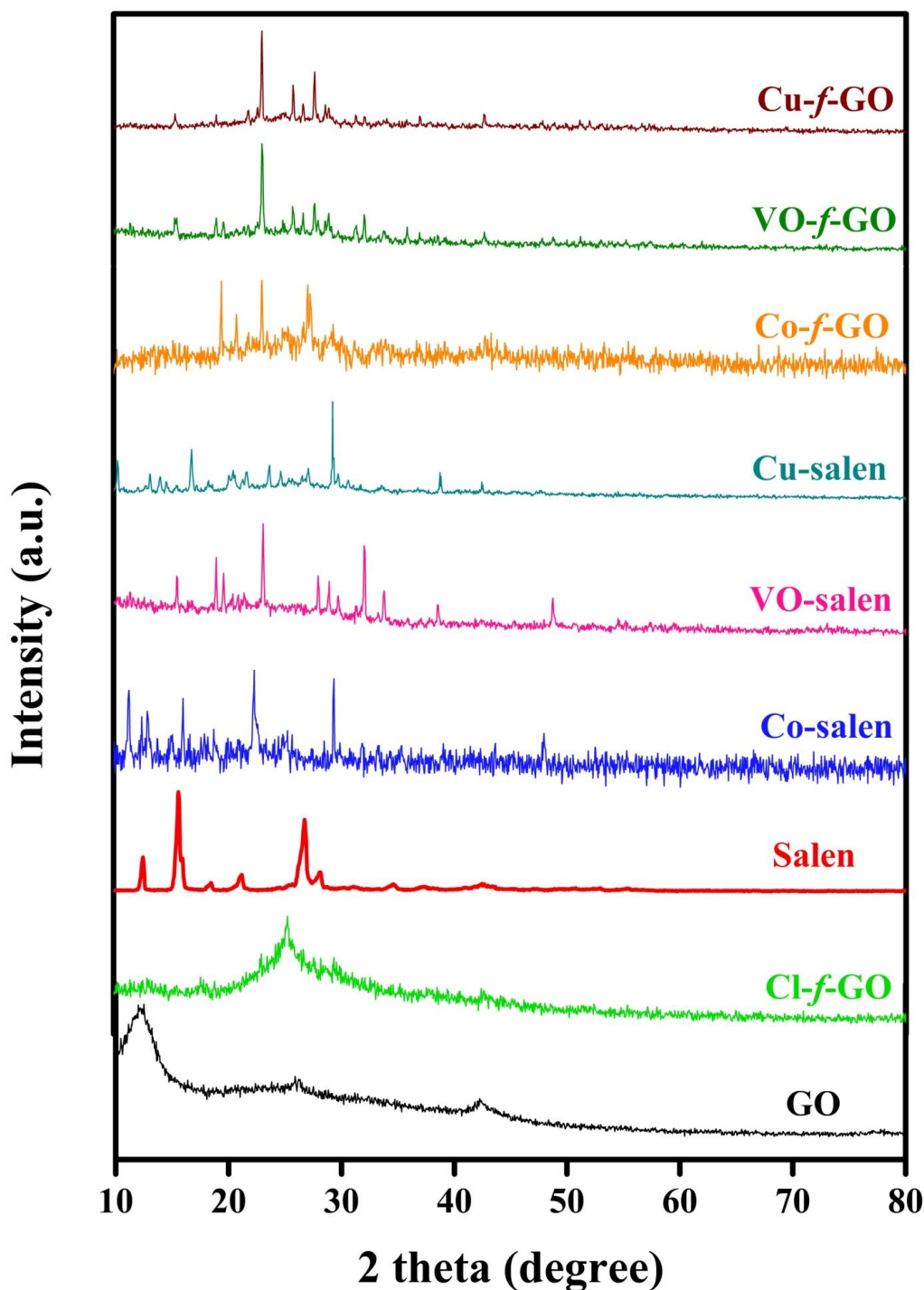


Fig. 3.20. XRD patterns of GO, Cl-f-GO, Salen, neat Co-salen, neat VO-salen, neat Cu-salen, Co-f-GO, VO-f-GO and Cu-f-GO.

3.2.6. XPS analysis

Fig. 3.21 demonstrates full range XPS survey spectra of GO, Co-f-GO, VO-f-GO and Cu-f-GO. It reveals that GO consists of simply C and O elements showing characteristic signals at 285.9 and 533.1 eV, while after

grafting with metal-salen complexes, the presence of N and metal particles are also documented in the XPS survey spectra of catalysts. A peak at 401.5 eV confirms the successful insertion of ligand, however, presence of metal ion is authenticate by promising peaks at different binding energy, for instance, peaks at 782.1, 531.2 and 933.5 eV are corresponds to Co2P, VO2P and Cu2P, respectively. This data confirms the successful grafting of ligand and metal complexes.

Moreover, high-resolution C1S spectra (Fig. 3.22A, 3.23A, 3.24A and 3.25A) demonstrates the bonding structure as C-C, alkoxy C-O, epoxy C-O-C, and ester and carboxy C=O observed at 284.5, 286.3, 288.2 and 289.2 eV, respectively in GO, as 284.6, 286.1, 286.7, 288.3 and 289.1 eV, respectively in Co-*f*-GO, as 284.5, 286.3, 286.7, 288.2 and 289.2 eV, respectively in VO-*f*-GO; as 284.6, 286.1, 286.7, 288.3 and 289.1 eV, respectively in Cu-*f*-GO; indicating successful oxidation of graphite by modified Hummers' method.

A change due to insertion of ligand is clearly visible in the high resolution C1S spectra of catalysts as reduction in peak at 286.3 eV and emergence of new peak at 286.7 eV signifying covalent attachment of N of ligand to the chloro-functionalized GO sheet¹⁷. Magnified view of N1S spectra of M-*f*-GO (M = Co²⁺, VO²⁺ and Cu²⁺) supports this covalent attachment by exhibiting peaks at 398.7 and 400.2eV in Co-*f*-GO, 398.8 and 400.2 eV in VO-*f*-GO while in Cu-*f*-GO it is observed at 398.8 and 400.3 eV which corresponds to non graphitic N, respectively⁵¹.

High resolution O1S spectra of GO (Fig. 3.22B) fitted into four peaks at 530.5, 531.6, 532.1 and 533.5 eV ascribing to quinines, C=O (carbonyl and carboxyl), C-O (epoxy and hydroxyl) and -OH, respectively. Whereas, magnified view of O1S spectra of M-*f*-GO (M = Co²⁺, VO²⁺ and Cu²⁺) (Fig. 3.23B, 3.24B and 3.25B) demonstrates a shifting of this peak to 533.9 eV due to coordination with metal ions.

The bonding energy of Co, VO and Cu metal is reflected in Fig. 3.23D, 3.24D and 3.25D, respectively. High resolution Co2p spectrum (Fig. 3.23D) demonstrates two contributions at 780.5 and 796.3 eV, originating from Co2p_{3/2} and Co2p_{1/2}, respectively. Additional peaks at 786.4 and 803.01 eV are ascribed to the “shake up” satellite peak exposing the existence of Co as Co₃O₄^{25, 52}. For VO, peaks observed at 516.1 and 523.7 eV are corresponds to

VO $2p_{3/2}$ and VO $2p_{1/2}$ (Fig. 3.24D) while the O1S peaks are observed at 530.1 and 532.2 eV confirming the presence of VO ion as VO_3O_4 . However, the “shake-up” satellites at 941.8 and 962.1 eV in the Cu 2p XPS spectrum (Fig. 3.25D) confirms the existence of $Cu^{2+53,54}$. In addition to this, two distinct peaks at 933.5 and 952.8 eV are attributed to Cu $2p_{3/2}$ and Cu $2p_{1/2}$, respectively. This spin-orbit-coupled Cu2p region demonstrates the presence of Cu as $Cu^{1+55, 56}$. These results reveal the presence of VO as VO_3O_4 ; Co as Co_3O_4 and Cu as Cu_2O and CuO . These results are in good agreement with XRD data which also confirms the existence of VO_3O_4 , Co_3O_4 , Cu_2O and CuO .

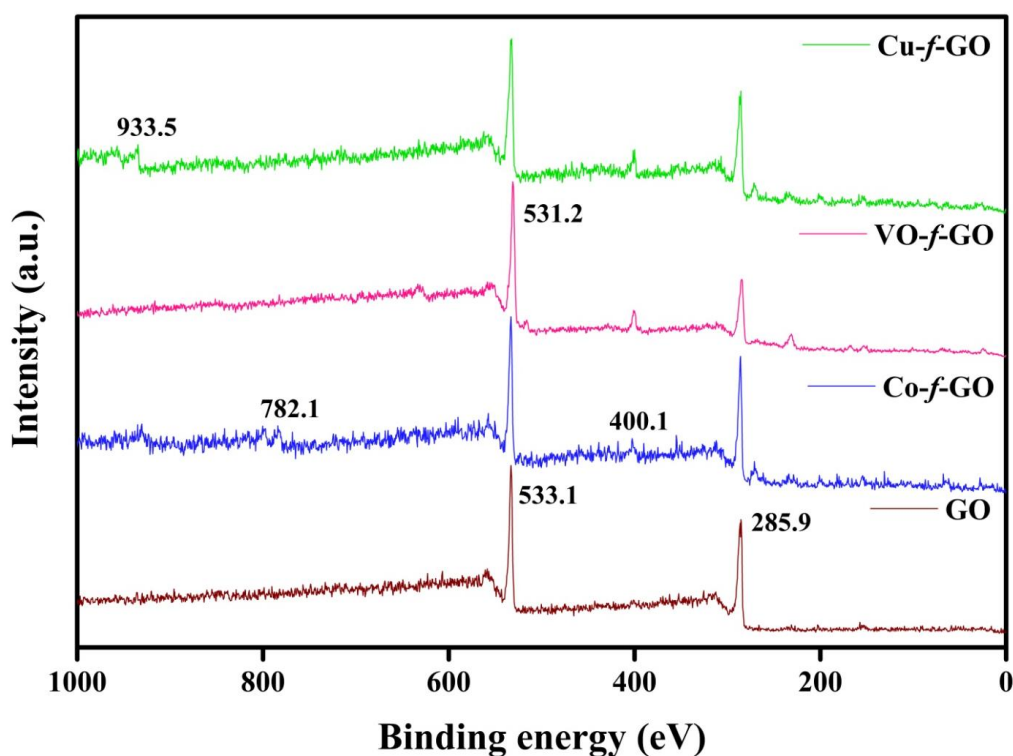


Fig. 3.21. Survey spectra of GO, Co-*f*-GO, VO-*f*-GO and Cu-*f*-GO.

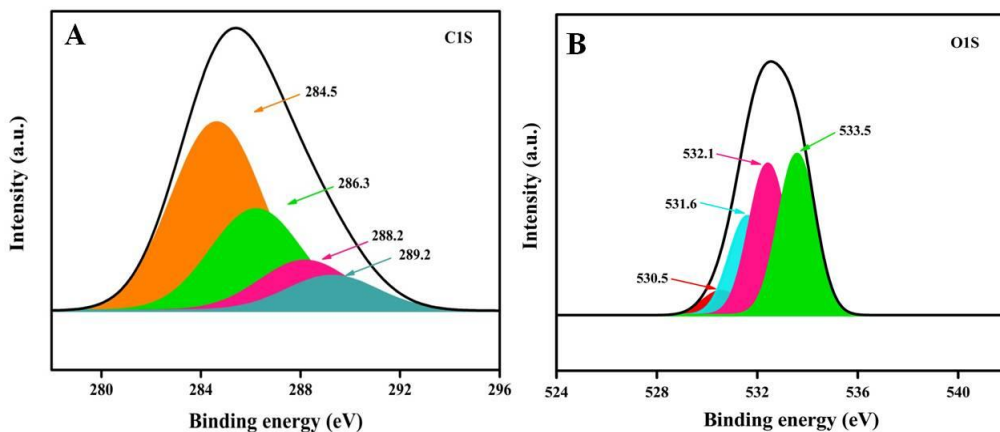


Fig. 3.22. High resolution XPS spectra of GO; (A) C 1S, (B) O 1S.

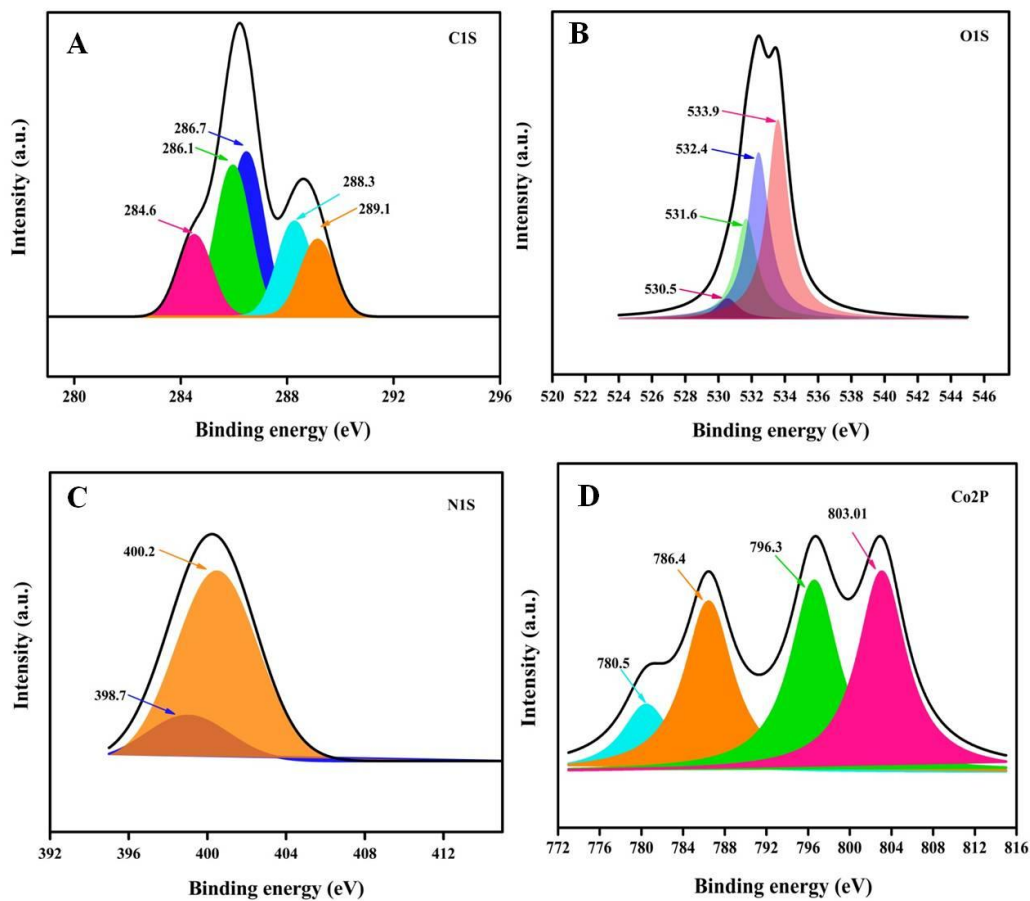


Fig. 3.23. High resolution XPS spectra of Co-f-GO; (A) C 1S, (B) O 1S, (C) N 1S and (D) Co2P.

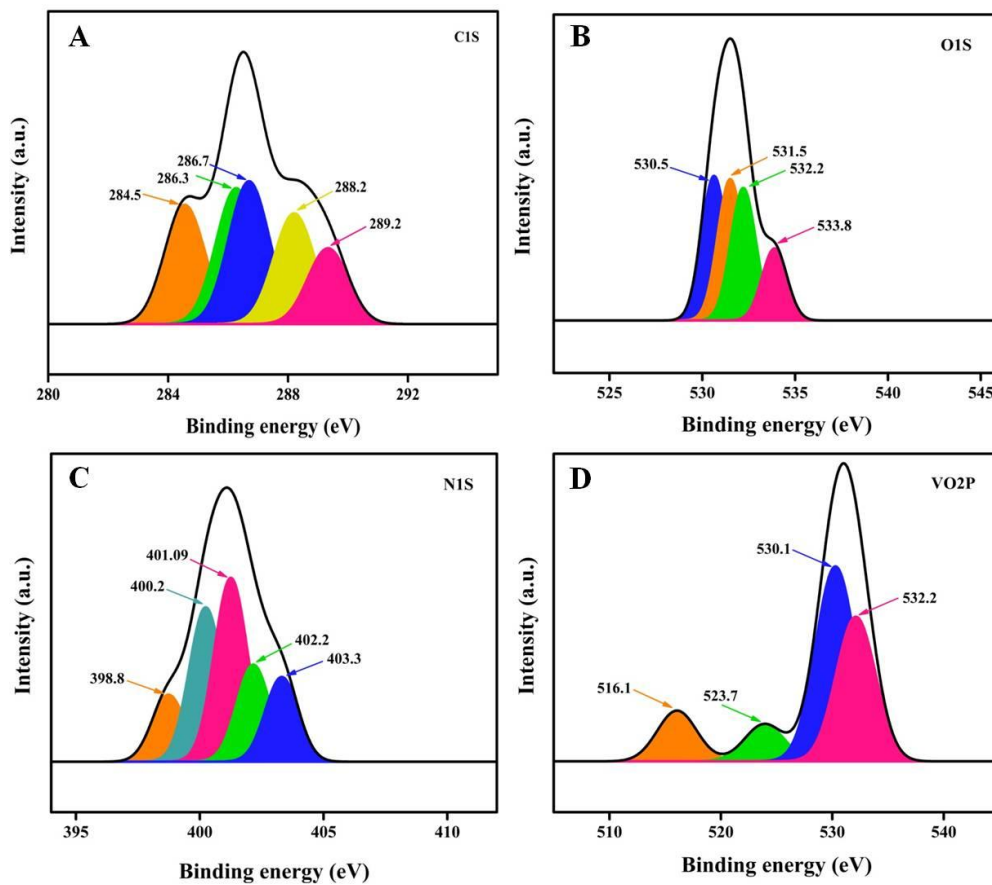


Fig. 3.24. High resolution XPS spectra of VO-*f*-GO; (A) C 1S, (B) O 1S, (C) N 1S and (D) VO₂P.

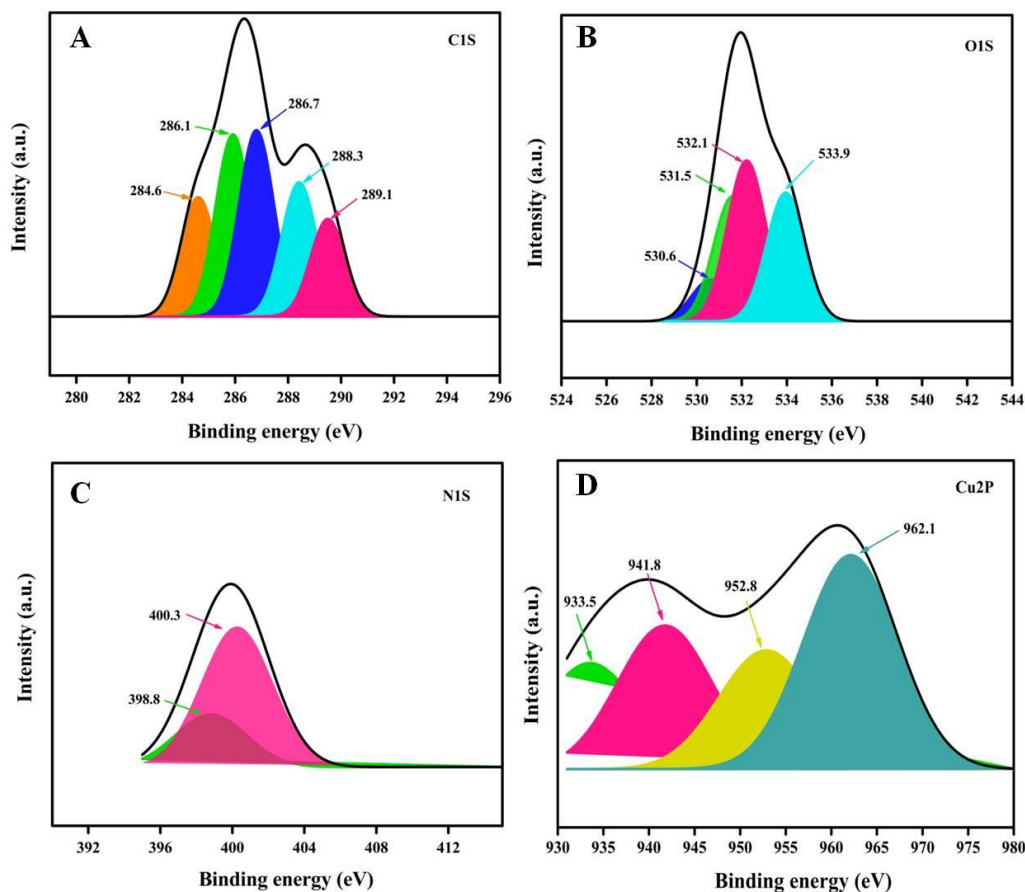


Fig. 3.25. High resolution XPS spectra of Cu-*f*-GO; (A) C 1S, (B) O 1S, (C) N 1S and (D) Co2P.

3.2.7. HRTEM analysis

As-prepared catalysts are examined through HRTEM analysis with SAED pattern (Fig. 3.26). Two-dimensional sheet-like structure of GO with 2-3 fold layered structure is clearly observed from Fig. 3.26(A). After functionalization with SOCl_2 , thickness of GO at the edges further increases and on grafting with metal ions more layered structure with well-stacked packing of GO sheets is seen. HRTEM images of Cl-*f*-GO markedly reveal that functionalization with SOCl_2 increases roughness of the surface indicating development of defects which is in concord with Raman analysis. Contrary to this, grafting of metal ions lessen the amorphicity of the samples showing the polycrystalline nature. The SAED pattern of GO [Fig. 3.26(D)] reveals the amorphous nature of the GO nanosheet²⁸. On the other hand, SAED pattern of Cl-*f*-GO, Co-*f*-GO, VO-*f*-GO and Cu-*f*-GO exhibits poorly visible dots signifying the polycrystalline nature of the samples. These data are in good

agreement with XRD results. The particle size calculated using Image J software for Co-*f*-GO, VO-*f*-GO and Cu-*f*-GO is 3.37 ± 1.1 , 2.69 ± 0.95 and 3.28 ± 0.10 nm, respectively [Fig. 3.26(U, V and W)].

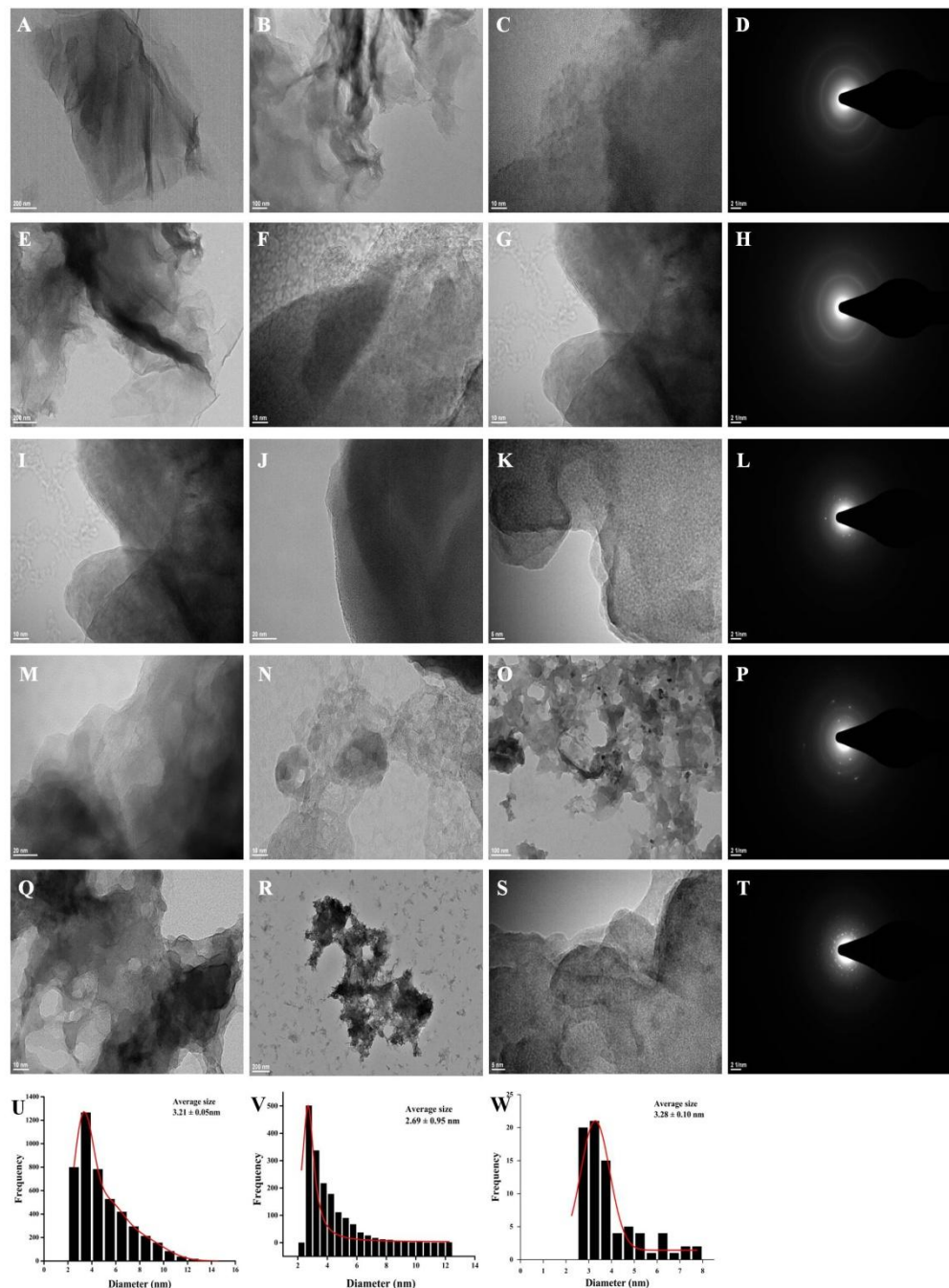


Fig. 3.26. HRTEM images of GO (A-C), Cl-*f*-GO (E-G), Co-*f*-GO (I-K), VO-*f*-GO (M-O), Cu-*f*-GO (Q-S), selected area electron diffraction (SAED) patterns of GO (D), Cl-*f*-GO (H), Co-*f*-GO (L), VO-*f*-GO (P) and Cu-*f*-GO (T) and average particle size distribution histograms of Co-*f*-GO (U), VO-*f*-GO (V), Cu-*f*-GO (W).

3.2.8. ICP-OES analysis

With the results of ICP-OES analysis, the metal content in as-synthesized catalysts has been estimated as 47.496, 35.39 and 32.397 ppm for Cu, V and Co, respectively. Metal loading per gram of catalysts is calculated using the formula: [Concentration of metal (ppm or mg/litre) x volume of the extract (litre)] / weight of the solid sample taken for extraction (gram)] to be 94.99, 70.78 and 64.79 mg/g for Cu-*f*-GO, VO-*f*-GO and Cu-*f*-GO, respectively.

3.2.9. NH₃-TPD study

Usually, temperature programmed desorption of ammonia (NH₃-TPD) method is characteristic tool to expose the distribution of acid site strength on the surface of solid heterogeneous catalysts. It gives an idea about acid properties like strength of acidic sites but cannot discriminate the Lewis and Brønsted acid sites. Low temperature peaks such as below 200 °C is assigned to mild acid sites, while peak at intermediate temperature range between 250-350 °C represents moderate acidic sites and peak at high temperature ascribes to strong acid sites.

Fig. 3.27 illustrates the sorption profiles of NH₃-TPD for the GO and Cl-*f*-GO. As can be seen from the figure several peaks are obtained at diverse temperature as a result of desorption of ammonia from the samples. In the sorption profile of GO peak exhibited at around 120 °C is seen to be shifted at around 102 °C in Cl-*f*-GO indicating the decrease in the adsorption of NH₃. However, GO shows another peak at around 346 °C representing second acidic site which is disappeared in Cl-*f*-GO. All these data confirms that insertion of chloro group onto the GO surface which has resulted in the rise of weak acid sites and diminish the strong acid sites.

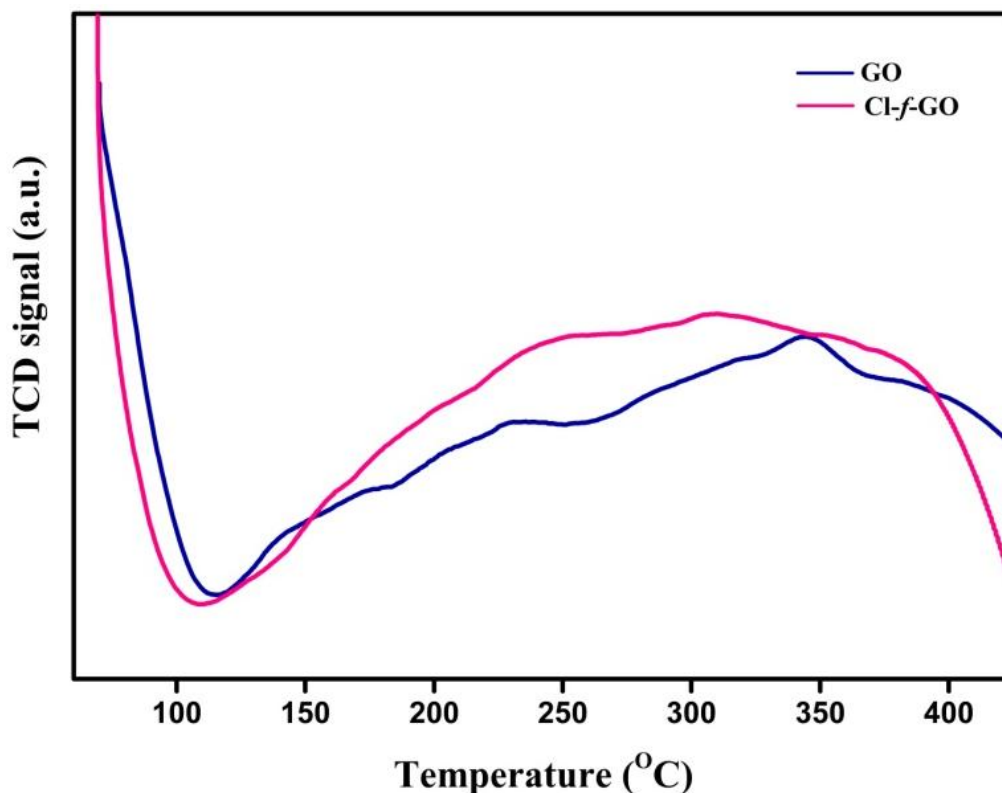


Fig. 3.27. NH_3 -TPD profile of catalysts GO and Cl-*f*-GO.

3.2.10. DFT study

In order to precisely investigate the structural and electronic properties, binding mechanism of a chlorinating reagent thionyl chloride (SOCl_2) over graphene with different functional groups like $-\text{O}-$, $-\text{OH}$ and $-\text{COOH}$, we have also performed first principles-based density functional theory (DFT) calculations. All DFT calculations to find the potential site for SOCl_2 are done in Gaussian09 program package⁵⁷ using well known hybrid functional namely Becke three parameters with Lee-Yang-Perdew correlation functionals (B3LYP) which is the mixture of Hartree-Fock (HF) exchange and DFT exchange-correlation functionals^{58,59}. The 6-31G basis set along with (d, p) polarization functions is utilized. The molecular orbitals (MO), highest occupied molecular orbitals (HOMO) and lowest unoccupied molecular orbitals (LUMO) are viewed through GaussView (version 5) using the outcomes of DFT calculations⁶⁰. Furthermore, we have re-optimized all calculations to achieve the same theoretical level of accuracy.

The binding energy (BE) of SOCl₂ over O-Graphene, OH-Graphene and COOH-Graphene is calculated through the following equation:

$$BE = E_{SOCl_2+(O/OH/COOH-Graphene)} - (E_{SOCl_2} + E_{(O/OH/COOH-Graphene)}) \quad (1)$$

Where $E_{SOCl_2+(O/OH/COOH-Graphene)}$ is the optimized total energy of system in which SOCl₂ is adsorbed over -O-, -OH and -COOH functionalized graphene, respectively, E_{SOCl_2} is the optimized energy of SOCl₂, $E_{(O/OH/COOH-Graphene)}$ is the optimized energy of -O-, -OH and -COOH functionalized graphene. Through the definition, negative value of E_{ad} depicts an exothermic reaction.

Furthermore, to study the chemical reactivity of SOCl₂ on -O-, -OH and -COOH functionalized graphene, we have also calculated the global descriptors. Based on Koopman's theorem⁶¹, the different global reactivity descriptors, i.e., electronegativity (χ), chemical potential (μ), global hardness (η), global electrophilicity index (ω) and global softness (S) are calculated using frontier molecular orbitals energies, E_{LUMO} , E_{HOMO} and are given by through below equations^{62,63};

$$\chi = -\frac{1}{2} (\epsilon_{HOMO} + \epsilon_{LUMO}) \quad (2)$$

$$\mu = -\chi = \frac{1}{2} (\epsilon_{HOMO} + \epsilon_{LUMO}) \quad (3)$$

$$\eta = \frac{1}{2} (\epsilon_{LUMO} - \epsilon_{HOMO}) \quad (4)$$

$$S = \frac{1}{2\eta} \quad (5)$$

$$\omega = \frac{\mu^2}{2\eta} \quad (6)$$

$$\Delta N_{max} = -\frac{\mu}{\eta} \quad (7)$$

The structural properties of SOCl₂ adsorbed over -O-, -OH and -COOH functionalized graphene have been studied in order to gain the detailed arrangement of constituent atoms/molecules in the combined systems. Fig. 3.28 presents top and side view of the initial structures of SOCl₂ adsorbed -O-, -OH and -COOH functionalized graphene. The thionyl chloride molecule is placed parallel at a distance of 2 Å on all -O-, -OH and -COOH

functionalized graphene. Furthermore, the SOCl_2 is positioned over the functional groups of graphene to provide the greater access and maximum effect. Fig. 3.28 shows the optimized structures of SOCl_2 over $-\text{O}-$, $-\text{OH}$ and $-\text{COOH}$ functionalized graphene. In all cases, after the optimization, SOCl_2 molecule is reoriented with sulphur atom facing the functionalized graphene sheet depicting its affinity towards the structural defects. Our calculated structural properties are in good agreement with other calculations in the literature⁶⁴. The equilibrium S-O bond distances are 2.87 Å and 6.39 Å in case of O-Graphene as shown in Fig. 3.29(a). In OH-Graphene, the S-O bond distance reduces to 2.72 Å. However, in COOH-Graphene, the partial bond is formed between H-Cl with the bond distance of 2.42 Å, which is even smaller than S-O bond distance in other two systems (Fig. 3.29(c)).

This alteration in structural parameters through binding will affect the electronic properties in all systems. The binding energy is determined through the formula given in Eq. (1). The lowest binding energy for SOCl_2 is found for O-Graphene (-0.206 eV) presented in Table 3.3. The binding energy for OH-Graphene and COOH-Graphene is almost similar with the values of -0.30 eV and -0.297 eV, respectively. The binding energy follows the sequence: OH-Graphene+ SOCl_2 > COOH-Graphene+ SOCl_2 > O-Graphene+ SOCl_2 . Although the binding energies are almost similar in both OH-Graphene and COOH-Graphene, but as can be seen from Fig. 3.29(b-c), the partial bond distance between H-Cl (in COOH-Graphene) is much lower than S-O (in OH-Graphene). This suggests that the $-\text{OH}$ group of carboxyl group at edge site prefers to bind or replace through chlorine of SOCl_2 as compared to S-O bonding in basal plane of OH-Graphene. The calculated binding energy through DFT is in good agreement with our own experimental results presented above. Further, we have also calculated Raman spectra of pristine and COOH-Graphene+ SOCl_2 as SOCl_2 presents superior binding over COOH-Graphene and is in agreement with our experimental study. The stability of COOH-Graphene+ SOCl_2 is also confirmed through the frequency calculation which shows the positive values of all acquired frequencies. The Raman spectra presented in Fig. 3.30 for COOH-Graphene+ SOCl_2 depicts the most intense peaks at 1381 and 1624 cm^{-1} which are D and G bands whereas for pristine the peaks are at 1390 cm^{-1} and 1624 cm^{-1} . The D and G bands are due

to edge defects of finite crystalline size and carbon-carbon bond stretching. The theoretical *ID/IG* ratios are found to be 1.40 and 1.3 for COOH-Graphene+SOCl₂ and COOH-Graphene, respectively, confirming good agreement with our experimental results.

To have an idea of chemical reactivity and site selectivity of SOCl₂ over -O-, -OH and -COOH functionalized graphene, we have evaluated electronegativity (χ), global hardness (η) and softness (S) values, electrophilicity index (ω), chemical potential (μ) and additional electronic charge (ΔN) from the neighbouring atoms using Koopman's theorem and are presented in Table 3.4. For a system to be good electrophile it should consists of high values of μ and ω , however, for nucleophile in nature low values of μ and ω are essential. As stated by maximum hardness principle, the most stable structure comprises maximum hardness. Table 3.4 presents interaction between SOCl₂ and OH-Graphene results in high value of global hardness indicating their strong interaction. The electrophilicity index (ω) examines the stabilization energy when a certain system acquires an extra charge from the surrounding. The large value of ω in OH-Graphene+SOCl₂ indicates its strong electrophile nature as compared to other systems. The chemical potential presents the trail of charge transfer functioning as an electrophile. Consequently, its μ must be negative. Our calculated μ is negative in all cases.

Intending to provide enlightenment between structural and electronic properties, the contour plots of highest occupied molecular orbitals (HOMO) and lowest unoccupied molecular orbitals (LUMO) are presented in Fig. 3.31. The HOMO and LUMO depicts electronic nature of molecules and are important in defining its chemical stability⁶⁵. The possibility to give out an electron is given by HOMO while the possibility to take an electron is provided through LUMO levels. The red colour presents positive and green colour presents negative phases of SOCl₂ over -O-, -OH and -COOH functionalized graphene. As seen in Fig. 3.31, in O-Graphene+SOCl₂, the delocalized π -bonds are distributed over the plane for HOMO. However, SOCl₂ weakens the uniformity of π -conjugated system and therefore, we can see the characteristics of σ orbit. However, in case of COOH-Graphene+SOCl₂, the HOMO is spread almost on entire sheet while LUMO

resides only on SOCl₂ molecule. The energy gap is calculated through the equation, $E_g = E_{LUMO} - E_{HOMO}$. After the adsorption of SOCl₂ molecule, the band gap increases in OH-Graphene. However, for other two O-Graphene and COOH-Graphene, the band gaps are reduced. For the demonstration of SOCl₂ effect over -O-, -OH and -COOH functionalized graphene, we also plots the density of states (DOS) as shown in Fig 3.32. The plotted curves for the DOS are derived from the distribution of MO energy levels in Multiwfn package⁶⁶. The vertical lines depict the position of HOMO level in considered systems. The DOS is plotted with the Gaussian width of 0.05 a.u. No obvious change in the HOMO level is observed in O-Graphene and COOH-Graphene with SOCl₂, however, noticeable changes are observed in OH-Graphene+SOCl₂ as compared to OH-Graphene resulting in the low binding energies. In summary, our DFT calculation which is in good agreement with our own experimental results shows that the chlorine of SOCl₂ prefers to be with -OH group of COOH-Graphene as well as surface hydroxyl groups.

Table 3.3

Calculated HOMO, LUMO, Energy band gap (E_g) and adsorption energy (E_{ad}) of all considered systems

System	HOMO (eV)	LUMO (eV)	E_g (eV)	E_{ad} (eV)
O-Graphene	-4.503	-2.666	1.837	-
O-Graphene + SOCl ₂	-4.677	-2.848	1.829	-0.206
OH-Graphene	-3.826	-3.430	0.396	-
OH-Graphene + SOCl ₂	-4.010	-3.594	0.416	-0.30
COOH-Graphene	-4.365	-2.092	2.272	-
COOH- Graphene+SOCl ₂	-4.462	-3.379	1.082	-0.297

Table 3.4

Calculated electronegativity (χ), chemical potential (μ), global hardness (η) and softness (S), global electrophilicity index (ω), additional electronic charge (ΔN_{\max}) of all considered systems.

Systems	χ (eV)	μ (eV)	η (eV)	S (1/eV)	ω (eV)	ΔN_{\max} (eV)
O-Graphene	3.58	-3.58	0.92	0.544	6.97	3.89
O-Graphene + SOCl ₂	3.76	-3.76	0.91	0.546	7.729	4.13
OH-Graphene	3.62	-3.62	0.19	2.52	33.09	19.05
OH-Graphene + SOCl ₂	3.80	-3.80	0.208	2.403	34.74	18.27
COOH-Graphene	3.22	-3.22	1.136	0.44	4.56	2.834
COOH- Graphene+SOCl ₂	3.92	-3.92	0.54	0.924	14.2	7.25

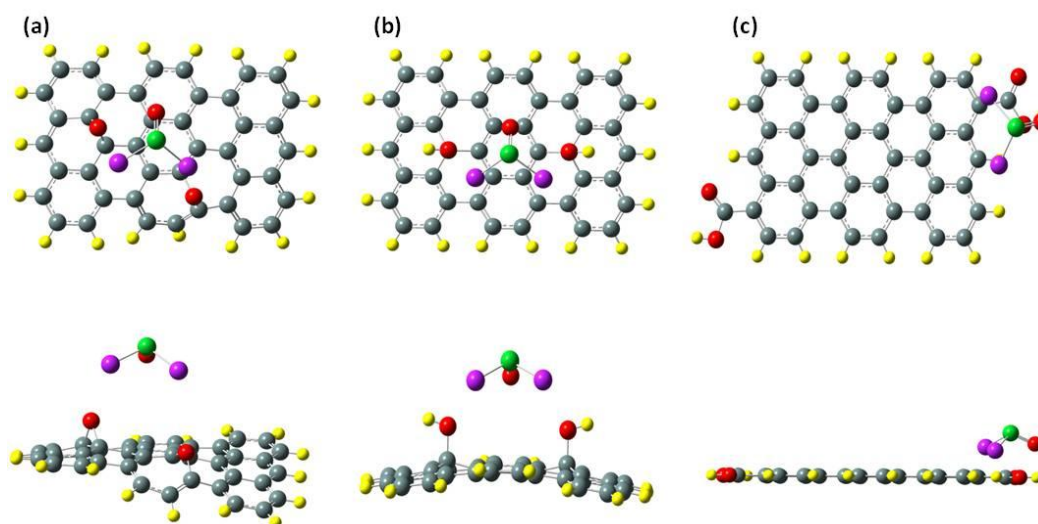


Fig. 3.28. Initial structures of SOCl₂ over (a) O-Graphene (b) OH- Graphene and (c) COOH- Graphene. Grey, yellow, red, purple and green colour presents carbon, hydrogen, oxygen, chlorine and sulphur atoms respectively.

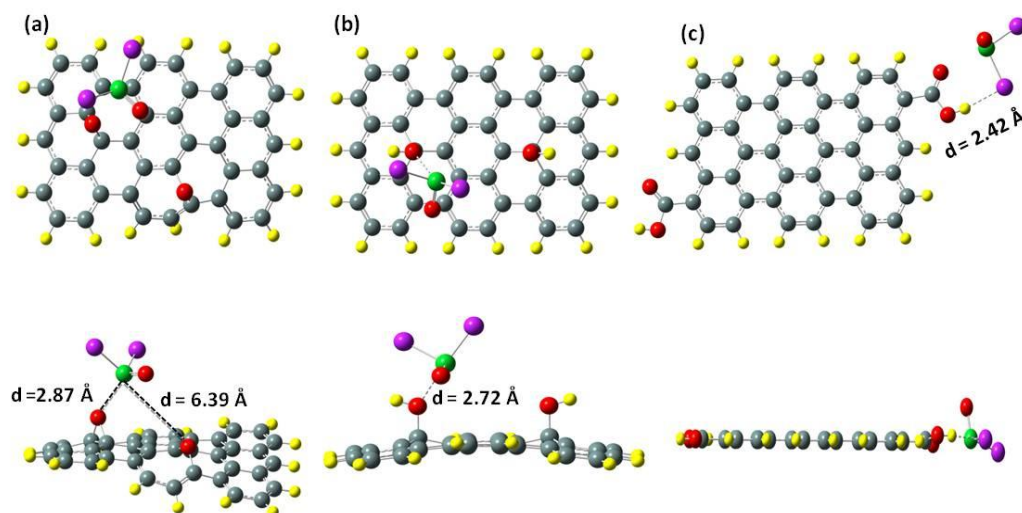


Fig. 3.29. Optimized structures SOCl_2 over (a) O-Graphene (b) OH- Graphene and (c) COOH- Graphene. Grey, yellow, red, purple and green colour presents carbon, hydrogen, oxygen, chlorine and sulphur atoms respectively.

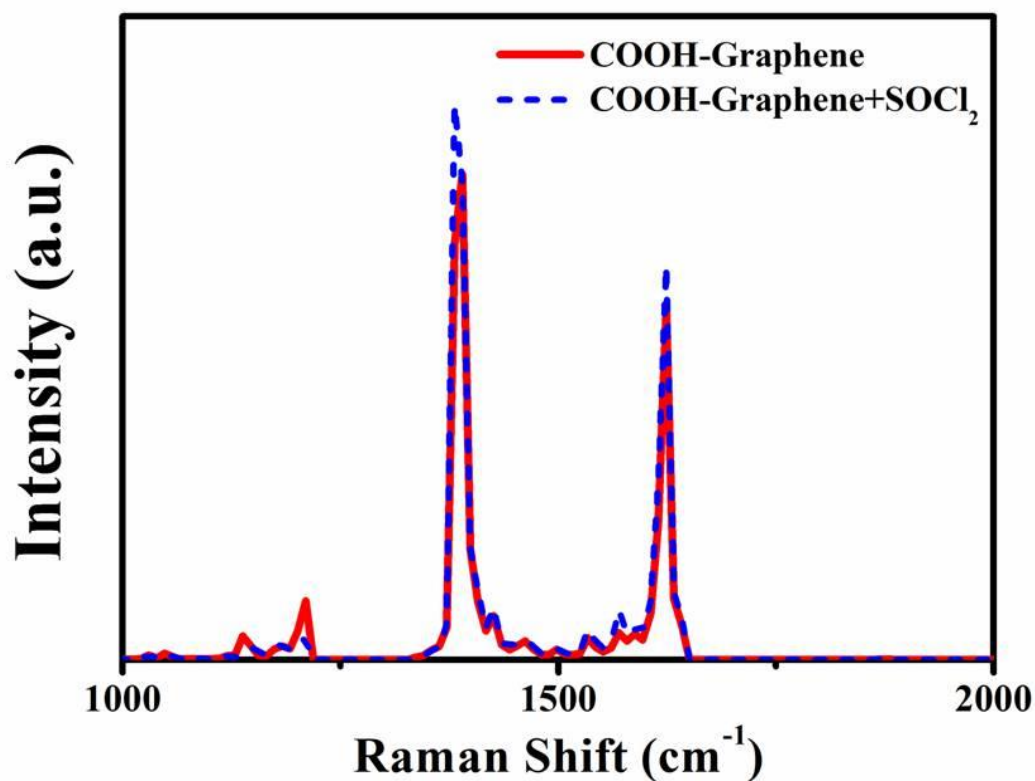


Fig. 3.30. Theoretical Raman spectra of pristine and SOCl_2 over COOH functionalized graphene.

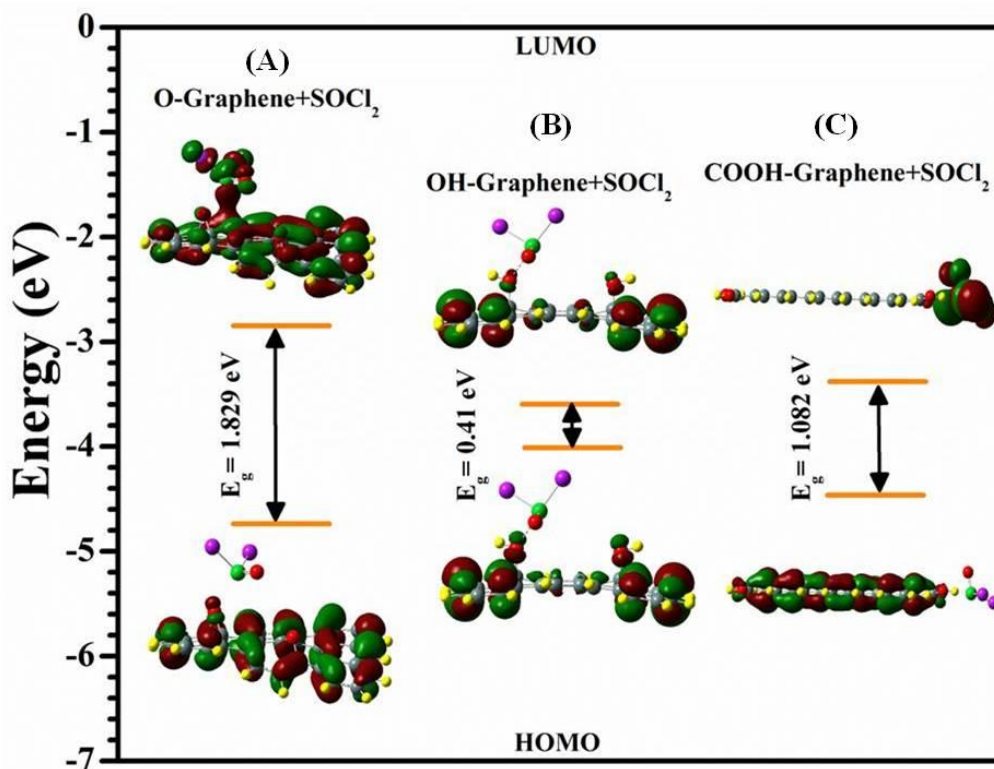


Fig. 3.31. HOMO-LUMO plots of SOCl₂ over (a) -O-Graphene (b) -OH-Graphene and (c) -COOH-Graphene.

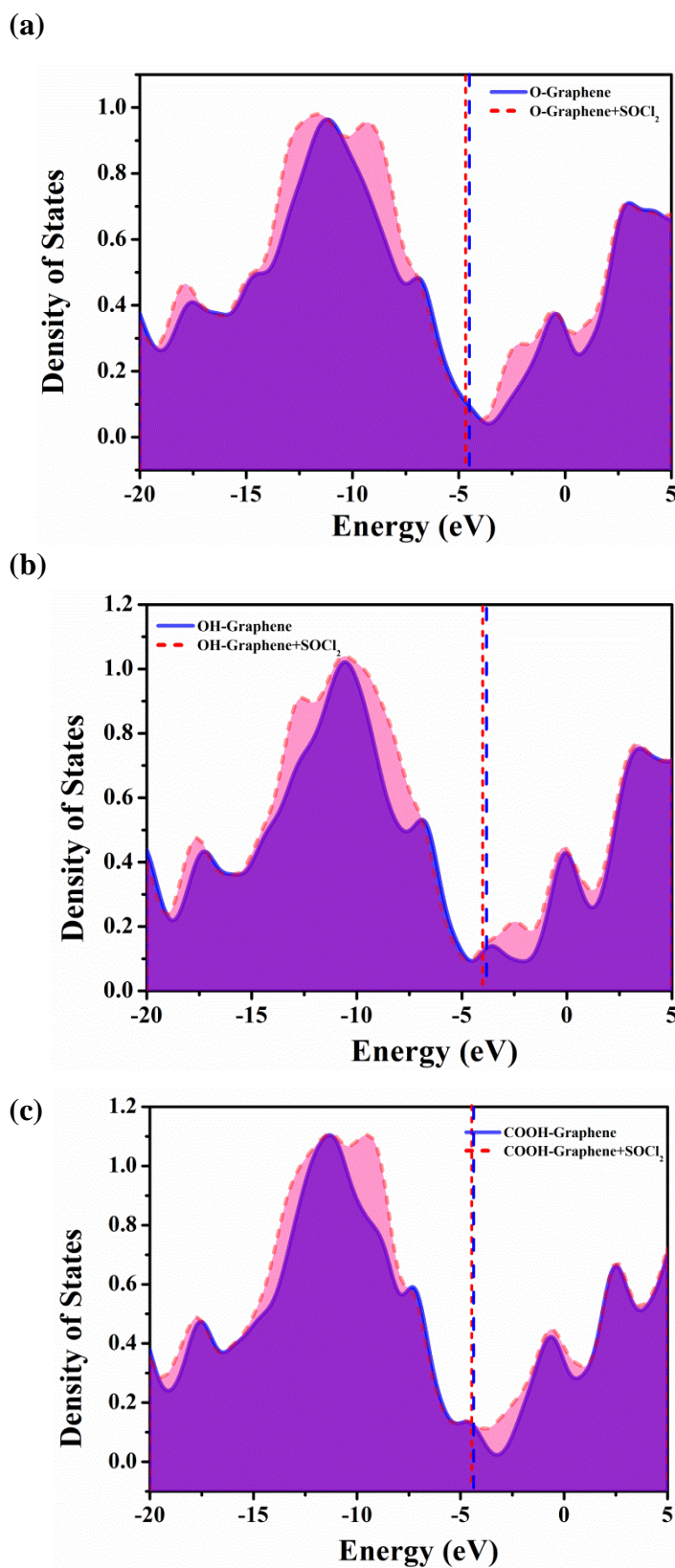


Fig. 3.32. Density of states (DOS) of (a) pristine and SOCl_2 adsorbed O-Graphene, (b) pristine and SOCl_2 adsorbed OH-Graphene and (c) pristine and SOCl_2 adsorbed COOH-Graphene.

3.3. References

1. J. F. Shen, B. Yan, M. Shi, H. W. Ma, N. Li and M. X. Ye, *J. Mater. Chem.*, 2011, **21(10)**, 3415-3421.
2. L. Li, Y. Y. Dou, L. F. Wang, M. Luo and J. Liang, *RSC Adv.*, 2014, **4(49)**, 25658-25665.
3. X. Ou, L. Jiang, P. Chen, M. Zhu, W. Hu, M. Liu, J. Zhu and H. Ju, *Adv. Funct. Mater.*, 2013, **23(19)**, 2422-2435.
4. T. Hemraj-Benny and S. S. Wong, *Chem. Mater.*, 2006, **18(20)**, 4827-4839.
5. J. Ou, J. Wang, S. Liu, B. Mu, J. Ren, H. Wang and S. Yang, *Langmuir*, 2010, **26(20)**, 15830-15836.
6. C. K. Modi, S. H. Patel and M. N. Patel, *J. Therm. Anal. Calorim.*, 2007, **87(2)**, 441-448.
7. G. Eda, Y. Lin, C. Mattevi, H. Yamaguchi, H. Chen, I. Chen, C. Chen and M. Chhowalla, *Adv. Mater.*, 2010, **22(4)**, 505-509.
8. H. Chang, Z. Sun, Q. Yuan, F. Ding, X. Tao, F. Yan and Z. Zheng, *Adv. Mater.*, 2010, **22(43)**, 4872-4876.
9. B. Zhou, X. Qian, M. Li, J. Ma, L. Liu, C. Hu, Z. Xu, X. Jiao, *J. Nanopart. Res.*, 2015, **17**, 130-141.
10. A. C. Ferrari, J. C. Meyer, V. Scardaci, C. Casiraghi, M. Lazzeri, F. Mauri, S. Piscanec, D. Jiang, K. S. Novoselov, S. Roth and A. K. Geim, *Phys. Rev. Lett.*, 2006, **97(18)**, 187401-187404.
11. C. N. R. Rao, A. K. Sood, R. Voggu and K. S. Subrahmanyam, *J. Phys. Chem. Lett.*, 2010, **1(2)**, 572-580.
12. K. Zhang, Y. Zhang and S. Wang, *Sci. Rep.*, 2013, **3**, 3448-3454.
13. A. K. Manna and K. S. Pati, *Chem. Asian J.*, 2009, **4**, 855-860.
14. N. Díez, A. Śliwak, S. Gryglewicz, B. Grzyb and G. Z. *RSC Adv.*, 2015, **5(100)**, 81831-81837.
15. N. M. El-Shafai, M. E. El-Khouly, M. El-Kemary, M. S. Ramadan and M. S. Masoud, *RSC Adv.*, 2018, **8**, 13323-13332.
16. B. Yuan, C. Bao, X. Qian, P. Wen, W. Xing, L. Song and Y. Hu, *Mater. Res. Bull.*, 2014, **55**, 48-52.
17. C. Su and K. P. Loh, *Acc. Chem. Res.*, 2012, **46(10)**, 2275-2285.
18. J. Liang and L. Li, *J. Mater. Chem. A*, 2017, **5**, 10998-11008.

19. R. Vithalani, D. Patel, C. K. Modi, N. N. Som, P. K. Jha and S. R. Kane, *Diamond & Related Materials*, 2018, **90**, 154-165.
20. R. Zou, K. Xu, T. Wang, G. He, Q. Liu, X. Liu, Z. Zhang and J. Hu, *J. Mater. Chem. A*, 2013, **1**, 8560-6.
21. T. Ghodselahi, M. A. Vesaghi, A. Shafiekhani, A. Baghizadeh and M. Lameii, *Appl. Surf. Sci.*, 2008, **255**, 2730-4.
22. J. S. Shaikh, R. C. Pawar, A. V. Moholkar, J. H. Kim, and P. S. Patil, *Appl. Surf. Sci.*, 2011, **257**, 4389-97.
23. K. Wang, X. Dong, C. Zhao, X. Qian and Y. Xu, *Electrochim. Acta.*, 2015, **152**, 433-42.
24. Y. C. Zhang, J. Y. Tang, G. L. Wang, M. Zhang and X. Y. Hu, *J. Cryst. Growth*, 2006, **294**, 278-82.
25. H. Xia, D. Zhu, Z. Luo, Y. Yu, X. Shi, G. Yuan and J. Xie, *Sci. Rep.*, 2013, **3**, 2978 (1-8).
26. S. N. Alam, N. Sharma and L. Kumar, *Scientific Research Publishing*, 2017, **6(1)**, 1-18.
27. X. J. Feng and L. Jiang, *Adv. Mater.*, 2006, **18**, 3063-3078.
28. G. X. Wang, J. Yang, J. Park, X. L. Gou, B. Wang, H. Liu and J. Yao, *J. Phys. Chem. C*, 2008, **112**, 8192-8195.
29. S. Sharma, M. N. Groves, J. Fennell, N. Soin, S. L. Horswell and C. Malardier-Jugroot, *Chem. Mater.*, 2014, **26(21)**, 6142-6151.
30. W. Zhang, V. Carravetta, Z. Li, Y. Luo and J. Yang, *J. Chem. Phys.*, 2009, **131(24)**, 244505-244506.
31. C. K. Modi, R. S. Vithalani, D. S. Patel, N. N. Som, P. K. Jha, *Microporous Mesoporous Mater.*, 2018, **261**, 275-285.
32. S. D. Dabhi, P. K. Jha, *Phys. E Low-Dimensional Syst. Nanostructures.*, 2017, **93**, 332-338.
33. M. C. Vu, G. D. Park, Y. H. Bae and S. R. Kim, *Polymer (Korea)*, 2016, **40(5)**, 804-812.
34. S. Samal, R. K. Acharya, and A. R. R. Dey, *J. Appl. Polym. Sci.*, 2003, **88**, 570-481.
35. N. Charef, L. Arrar, A. Ourari, R. M. Zalloum, and M. S. Mubarak, *J. Macromol. Sci. A: Pure and Appl. Chem.*, 2010, **47**, 177-184.
36. G. S. V. Kumar and B. Mathew, *J. Appl. Polym. Sci.*, 2004, **92**, 1271-1278.

37. Y. Li, N. Yang, T. Du, X. Wang and W. Chen, *Water Research*, 2016, **103**, 416-423.
38. D. A. Dikin, S. Stankovich, E. J. Zimney, R. D. Piner, G. H. B. Dommett, G. Evmenenko, S. T. Nguyen and R. S. Ruoff, *Nature*, 2007, **448**, 457-460.
39. S. Park, K. S. Lee, G. Bozoklu, W. Cai, S. T. Nguyen and R. S. Ruoff. *ACS Nano*, 2008, **2**, 572-578.
40. S. Stankovich, D. A. Dikin, O. C. Compton, G. H. B. Dommett, R. S. Ruoff and S. T. Nguyen, *Chem. Mater.*, 2010, **22**, 4153-4157.
41. L. M. Fostiak, I. García, J. K. Swearingen, E. Bermejo, A. Castiñeiras and D. X. West, *Polyhedron*, 2003, **22**, 83-92.
42. N. K. Ngan, K. M. Lo and C. S. R. Wong, *Polyhedron*, 2012, **33**, 235-251.
43. P. Krishnamoorthy, P. Sathyadevi, A. H. Cowley, R. R. Butorac and N. Dharmaraj, *Eur. J. Med. Chem.*, 2011, **46**, 3376-3387.
44. T. Ghosh, S. Bhattacharya, A. Das, G. Mukherjee and M. G. Drew, *Inorg. Chim. Acta*, 2005, **358**, 989-996.
45. Y. Zhu, S. Murali, W. Cai, X. Li, J. W. Suk, J. R. Potts and R. S. Ruoff, *Adv. Mater.*, 2010, **22**, 3906-3924.
46. N. Diez, A. Śliwak, S. Gryglewicz, B. Grzyb and G. Z. Gryglewicz, *RSC Adv.*, 2015, **5(100)**, 81831-81837.
47. B. Zhang, H. Su, X. Gu, Y. Zhang, P. Wang, X. Li, X. Zhang, H. Wang, X. Yang, S. Zeng, *Catal. Sci. Technol.*, 2013, **3(10)**, 2639-2645.
48. J. Xie, C. Wu, S. Hu, J. Dai, N. Zhang, J. Feng, J. Yang and Y. Xie, *Phys. Chem. Chem. Phys.*, 2012, **14(14)**, 4810-4816.
49. A. K. Sasmal, S. Dutta and T. Pal, *Dalton Transactions*, 2016, **45(7)**, 3139-3150.
50. M. Kuang, T. T. Li, H. Chen, S. M. Zhang, L. L. Zhang and Y. X. Zhang, *Nanotechnology*, 2015, **26**, 304002.
51. S. S. K. Mallineni, S. Bhattacharya, F. Liu, P. Puneet, A. Rao, A. Srivastava and R. Podila, 'Two-dimensional materials - synthesis, characterization and potential applications' in P. K. Nayak, *Defect engineered 2D materials for energy applications*, IntechOpen, Chap-5, 2016, pp. 83-102.

52. L. Zhang, X. Zhao, W. Ma, M. Wu, N. Qian and W. Lu, *Cryst. Eng. Comm.*, 2013, **15**, 1389-1396.
53. T. Ghodselahi, M. A. Vesaghi, A. Shafiekhani, A. Baghizadeh and M. Lameii, *Appl. Surf. Sci.*, 2008, **255**, 2730-2734.
54. J. S. Shaikh, R. C. Pawar, A. V. Moholkar, J. H. Kim and P. S. Patil, *Appl. Surf. Sci.*, 2011, **257**, 4389-4397.
55. K. Wang, X. Dong, C. Zhao, X. Qian and Y. Xu, *Electrochim. Acta.*, 2015, **152**, 433-442.
56. Y. C. Zhang, J. Y. Tang, G. L. Wang, M. Zhang and X. Y. Hu, *J. Cryst. Growth*, 2006, **294**, 278-282.
57. M. J. Frisch, G. W. Trucks, H. B. Schlegel, G. E. Scuseria, M. A. Robb, J. R. Cheeseman et al., GAUSSIAN 09 (Revision C.01), Gaussian, Inc., Wallingford, CT, 2010.
58. A. D. Becke, *Phys. Rev. A*, 1988, **38**, 3098.
59. C. Lee, W. Yang and R.G. Parr, *Phys. Rev. B*, 1988, **37**, 785.
60. R. Dennington, T. Keith, J. Millam, GaussView, version 5; Semichem Inc.: Shawnee Mission, KS, 2009.
61. R. G. Parr and W. Yang, *Density Functional Theory of Atoms and Molecules*, Oxford University Press: New York, 1989.
62. R. G. Pearson, *J. Org. Chem.*, 1989, **54**, 1423-1430.
63. R. G. Parr and R. G. Pearson, *J. Am. Chem. Soc.*, 1983, **105**, 7512-7516.
64. M. Breza, *THEOCHEM*, 2006, **767**, 159-163.
65. S. Gunasekaran, R. A. Balaji, S. Kumaresan, G. Anand and S. Srinivasan, *Can. J. Anal. Sci. Spectrosc.*, 2008, **53**, 149-162.
66. T. Lu and F. Chen, *J. Comput. Chem.*, 2012, **33**, 580-592.